

(Ni_{0.375}Cu_{0.375}Mg_{0.25})Al₂O₄ INTERNAL REFORMING CATALYST FOR
SOLID OXIDE FUEL CELL ANODES

BY

PETER J. SOWINSKI

A THESIS
SUBMITTED TO THE FACULTY OF

ALFRED UNIVERSITY

IN PARTIAL FULFILLMENT OF THE REQUIREMENTS
FOR THE DEGREE OF

MASTER OF SCIENCE

IN

MATERIALS SCIENCE AND ENGINEERING

ALFRED, NEW YORK

SEPTEMBER, 2016

(Ni_{0.375}Cu_{0.375}Mg_{0.25})Al₂O₄ INTERNAL REFORMING CATALYST FOR
SOLID OXIDE FUEL CELL ANODES

BY

PETER J. SOWINSKI

B.S. ALFRED UNIVERSITY (2014)

SIGNATURE OF AUTHOR _____

APPROVED BY _____

SCOTT T. MISTURE, ADVISOR

STEVEN M. PILGRIM, ADVISORY COMMITTEE

HERBERT GIESCHE, ADVISORY COMMITTEE

CHAIR, ORAL THESIS DEFENSE

ACCEPTED BY _____

ALASTAIR N. CORMACK, INTERIM DEAN
KAZUO INAMORI SCHOOL OF ENGINEERING

Alfred University theses are copyright protected and may be used for education or personal research only. Reproduction or distribution in part or whole is prohibited without written permission from the author.

Signature page may be viewed at Scholes Library,
New York State College of Ceramics, Alfred University,
Alfred, New York.

ACKNOWLEDGMENTS

This paper is a reflection of the hundreds of hours of successful experiments, but it does not begin to reflect the late nights spent studying for tests or finishing homework after long hours working for the athletic department, or the frustration of spending days preparing samples for the Probostat™ only to have erratic or no data to show for it. Graduate school has been many things but the one thing it has not been is easy, and without the people in my life that supported me along the way I know I could not have made it this far.

First and foremost, I need to thank my family: Mom, Dad, Abbey, Alicia, and Annie: your unconditional love and support has helped me to see this through.

Next I need to thank Tony Aquilina for allowing me the opportunity to be his graduate assistant which funded my graduate schooling. You taught me many valuable lessons and you are a great friend.

Dom Laurienzo, Sheldon Vosburgh, Kameron Chambliss, Rich Lenihan, Zac Toth, and Rob Locker: When we were together, shooting the breeze or goofing around, my frustrations and problems always faded away.

Ross Munson, you have been a coach, a counselor, and a great friend. We have been through a lot, from our unforgettable trip across the country to our talks where we solved the world's problems, and I cannot thank you enough.

To the other graduate students at AU: Trevyn Hey and Peter Metz from Café X-ray, Mike Alberga, Brittany Higgins, Alec Ladonis, Aubrey Fry, and all the others: Thank you for all the memorable days and late nights in the labs and offices, for our conversations related to engineering and those that weren't, for commiserating in our problems and reveling in our successes. It has been a fun trip together.

A huge thank you to Swavek Zdzieszynski, Gerry Wynick, and Fran Williams for training me on equipment, helping troubleshoot problems, and fixing things that I could not. This work could not have been done without you.

Finally, thank you to my advisor: Scott Mixture, committee members: Herbert Giesche and Steven Pilgrim, and Professors Bill Carty and Roger Loucks. You have all helped me through this process in various ways and I have learned much about engineering and life from all of you.

This work made use of the Cornell Center for Materials Research Shared Facilities which are supported through the NSF MRSEC program (DMR-1120296).

TABLE OF CONTENTS

	Page
Acknowledgments	iii
TABLE OF CONTENTS	iv
List of Tables	vi
List of Figures	vii
ABSTRACT	ix
INTRODUCTION	1
A. Fuel Cell Background	1
B. SOFC Fundamentals	2
1. Cathodes	3
2. Electrolytes	3
3. Anodes	4
C. Carbon Deposition	9
D. SOFC Power Measurements	11
1. Ohmic Polarization	12
2. Concentration Polarization	12
3. Activation Polarization	12
E. Spinel Catalysts	13
EXPERIMENTAL PROCEDURE	14
A. Powder Synthesis	14
B. Room Temperature X-ray Diffraction	15
C. High Temperature X-ray Diffraction Measurements for Coefficient of Thermal Expansion (CTE)	15
D. Phase Interaction Study	16
E. Fuel Cell Preparation	16
F. Electrochemical Performance	16
G. Scanning Electron Microscopy	18
H. Raman Spectroscopy	18
RESULTS	18
A. Phase Compatibility	18
1. $\text{Ni}_{0.375}\text{Cu}_{0.375}\text{Mg}_{0.25}\text{Al}_2\text{O}_4$ - NiO - YSZ	19

2. $\text{Ni}_{0.375}\text{Cu}_{0.375}\text{Mg}_{0.25}\text{Al}_2\text{O}_4$ - NiO – GDC	20
B. Coefficient of Thermal Expansion.....	21
C. Electrochemical Performance.....	23
D. Scanning Electron Microscopy.....	28
1. Fuel Cell With No Spinel Additions	28
2. Fuel Cell With 0.015g of Spinel Added.....	28
3. Fuel Cell With 0.05g of Spinel Added.....	30
E. Raman Spectroscopy	32
DISCUSSION	33
A. Phase Compatibility	33
B. Coefficient of Thermal Expansion (CTE)	34
C. Electrochemical Performance.....	35
1. Operation Under 4% H_2	35
2. Operation Under Methane-Carbon Dioxide Gas Mixtures	36
D. Scanning Electron Microscopy and Raman Spectra	38
SUMMARY AND CONCLUSIONS	39
FUTURE WORK	41
REFERENCES	42
APPENDICES	48
Appendix A. $\text{Ni}_{0.375}\text{Cu}_{0.375}\text{Mg}_{0.25}\text{Al}_2\text{O}_4$ XRD Pattern.....	48
Appendix B. Coefficient of Thermal Expansion	50
Appendix C. Electrochemical Performance Measurements.....	50
Appendix D. SEM Photomicrographs.....	52

LIST OF TABLES

	Page
Table I. Fuel Cell Types and Associated Characteristics	1
Table II. Summary of Potential Fuel Cell Materials with Operation Temperature and Associated Fuel Gas and Peak Power Densities	6
Table III. CTE of Fuel Cell Materials From 25°C to 1000°C and the Calculated CTE of Spinel From 25°C to 850°C	22

LIST OF FIGURES

	Page
Figure 1. Schematic of a fuel cell operating on a H ₂ and CO fuel gas and air as the oxidant.....	3
Figure 2. A representation of the spinel structure rendered using CrystalMaker software; yellow atoms occupy the A site, blue atoms occupy the B site, and red atoms represent oxygen.	13
Figure 3. Schematic of Probostat™ fuel cell testing apparatus (left) with enlarged fuel cell and current collector diagram (right).	17
Figure 4. XRD patterns for phase compatibility study of NiO-YSZ-Cu375. Spinel peak intensity increases while NiO peak intensity decreases, most obviously at 37° 2θ (Cu375) and 37.3° 2θ (NiO).	20
Figure 5. XRD patterns for NiO-GDC-Cu375 phase compatibility study. The spinel peaks show an increase in intensity as temperature increases concurrently with a decrease in intensity of the NiO peaks.....	21
Figure 6. Lattice parameter vs temperature for Ni _{0.375} Cu _{0.375} Mg _{0.25} Al ₂ O ₄	22
Figure 7. Lattice parameter vs temperature for Ni _{0.375} Cu _{0.375} Mg _{0.25} Al ₂ O ₄	22
Figure 8. Current density vs voltage and current density vs power density curves for a fuel cell (a) with 0.015g of spinel added and (b) without spinel added operating under 32% CH ₄ - 63% CO ₂ - 5% N ₂	26
Figure 9. Maximum power density at 850°C of a fuel cell with 0.015g of spinel added, a fuel cell with 0.05g of spinel added, and a fuel cell with no spinel addition..	27
Figure 10. Secondary electron image of the fuel cell anode that had no spinel additions on the surface.	28
Figure 11. BSE image of 0.015g of spinel (darkest particles) added onto a Ni-YSZ anode.	29
Figure 12. Backscattered electron image of spinel (dark particles), with nanoparticles on surface (bright spots), deposited on the Ni-YSZ anode.....	30

Figure 13. SEM photomicrograph of fuel cell anode with 0.05g of spinel added to the surface of the anode. Catalytically active nickel-copper nanoparticles (bright spots) can be seen on the surface of the spinel. 31

Figure 14. Backscattered electron image of a fuel cell with full spinel coverage after endurance testing. 31

Figure 15. Ex-situ Raman spectra for endurance testing fuel cell samples. 32

ABSTRACT

Nickel-based anodes are the most commonly used anodes for solid oxide fuel cell (SOFC). Unfortunately, with nickel based anodes, internal reforming of hydrocarbon fuels is often accompanied by carbon deposition, which covers the active nickel sites, resulting in degradation of cell performance. $\text{Ni}_{0.375}\text{Cu}_{0.375}\text{Mg}_{0.25}\text{Al}_2\text{O}_4$ spinel catalyst was investigated for its use as a potential internal reforming layer for SOFC anodes.

To determine if any reactions with NiO, $\text{Y}_{0.08}\text{Zr}_{0.92}\text{O}_2$ (YSZ), or $\text{Gd}_{0.2}\text{Ce}_{0.8}\text{O}_2$ (GDC) occur during fuel cell fabrication, $\text{Ni}_{0.375}\text{Cu}_{0.375}\text{Mg}_{0.25}\text{Al}_2\text{O}_4$ was thoroughly mixed with NiO-YSZ and NiO-GDC and fired at temperatures ranging from 1300°C - 1500°C. Room temperature X-ray powder diffraction of the samples revealed spinel peak shifts, indicating compositional changes towards a higher nickel concentration spinel.

Rietveld refinements of high temperature X-ray diffraction patterns were used to calculate the coefficient of thermal expansion of the spinel. With a calculated CTE of $10 \times 10^{-6} \text{ K}^{-1}$ from 25°C to 850°C, the CTE of the oxide spinel is at least 5% lower than Ni-YSZ, YSZ, and $\text{La}_{0.8}\text{Sr}_{0.2}\text{MnO}_3$ (LSM).

When 0.015g of spinel was added to the fuel cell anode, no change in the peak power density was observed while operating under hydrogen. However, 0.015g of spinel addition while operating under a non-coking methane fuel gas mixture caused an increase in peak power density from $74 \text{ mW}\cdot\text{cm}^{-2}$ to $98 \text{ mW}\cdot\text{cm}^{-2}$ (32% increase) at 850°C and $40 \text{ mW}\cdot\text{cm}^{-2}$ to $52 \text{ mW}\cdot\text{cm}^{-2}$ (31% increase) at 750°C.

After 50 hours operating on a coking methane fuel gas mixture at 850°C, a fuel cell with no spinel additions had a peak power density drop of approximately 16%. With 0.015g of added spinel, the peak power density degraded by a lesser amount, 10%. Finally, with 0.05 g of spinel added, the peak power density decreased by only 6%. After endurance testing, no carbon fibers were observed on the anode during SEM imaging. Raman shift shows the fingerprint graphitic carbon bands on the anode with no spinel additions, but not on the fuel cells with spinel additions.

Due to the coefficient of thermal expansion mismatch, $\text{Ni}_{0.375}\text{Cu}_{0.375}\text{Mg}_{0.25}\text{Al}_2\text{O}_4$ is not well suited for use as a reforming catalyst for high temperature SOFCs. However, it can be used in intermediate temperature fuel cells (IT-SOFCs). In addition, with optimization of the processing and application to the anode, $\text{Ni}_{0.375}\text{Cu}_{0.375}\text{Mg}_{0.25}\text{Al}_2\text{O}_4$ could eliminate the need for upstream fuel reforming in IT-SOFCs.

INTRODUCTION

A. Fuel Cell Background

Fuel cells are energy conversion devices that convert the chemical energy of fuel gases such as hydrogen (H₂), carbon monoxide (CO), and methane (CH₄) into electrical energy without the need for direct combustion as an intermediate step. Able to bypass direct combustion, fuel cells can produce electricity much more efficiently than traditional thermomechanical methods, which are limited by the Carnot cycle.¹

The origin of fuel cells lies in the middle of the 19th century when Sir William Grove developed what would later be referred to as the “Grove cell.” The Grove cell, which operated at room temperature with a dilute sulfuric acid electrolyte, a hydrogen anode, and an oxygen cathode, was based on the reverse electrolysis of water.²⁻⁴ However, ceramic fuel cells were not developed until the end of the 19th century when Nernst suggested in a patent that a solid electrolyte could be electrically conductive after heating from an auxiliary heat source.⁴ Since Sir William Grove developed his cell almost 180 years ago there have been eight major types of fuel cells developed. Each type of fuel cell

Table I. Fuel Cell Types and Associated Characteristics

Types of fuel cell	Electrolyte	Operating Temperature (°C)	Fuel	Oxidant	Efficiency
Alkaline (AFC)	potassium hydroxide (KOH)	50–200	pure hydrogen or hydrazine	O ₂ /Air	50–55%
Direct methanol (DMFC)	polymer	60–200	liquid methanol	O ₂ /Air	40–55%
Phosphoric acid (PAFC)	phosphoric acid	160–210	hydrogen from hydrocarbons and alcohol	O ₂ /Air	40–50%
Sulfuric acid (SAFC)	sulfuric acid	80–90	alcohol or impure hydrogen	O ₂ /Air	40–50%
Proton-exchange membrane (PEMFC)	polymer, proton exchange membrane	50–80	less pure hydrogen from hydrocarbons or methanol	O ₂ /Air	40–50%
Molten carbonate(MCFC)	molten salt such as nitrate, sulphate, carbonates...	630–650	hydrogen, carbon monoxide, natural gas, propane, other hydrocarbons	CO ₂ /O ₂ /Air	50–60%
Solid oxide (SOFC)	ceramic as stabilised zirconia and doped perovskite	600–1000	natural gas or propane	O ₂ /Air	45–60%, up to 90% with heat recovery systems
Protonic ceramic (PCFC)	thin membrane of barium cerium oxide	600–700	hydrocarbons	O ₂ /Air	45–60%

is characterized by the electrolyte that is used. The electrolyte material dictates the operating temperature as seen in Table I.²

Solid oxide fuel cells (SOFCs) have received a substantial amount of attention in recent history for the following reasons: ^{2,5,6}

- Fuel conversion efficiency in the range of 45-60% with standalone units, but when coupled with heat recovery systems the efficiency can be improved to almost 90%
- High operating temperatures make SOFCs fuel flexible; able to use hydrocarbon fuels such as natural gas means new infrastructures for producing, storing, and distributing fuels do not need to be developed or significantly improved upon
- SOFCs system size can be changed and adapted for particular needs ranging from large scale industrial size energy producing units to mobile units used in automotive applications
- Solid state construction permits handling and avoids problems with electrolyte management

B. SOFC Fundamentals

A SOFC has three major components: a cathode where molecular oxygen is reduced to O^{2-} ions, an ionically conductive electrolyte which transports the O^{2-} ions from the cathode to the anode, and an anode that catalyzes the oxidation of the incoming fuel to produce H_2O and CO_2 . Electrons flow from the anode to the cathode through an external circuit. Figure 1 depicts the operation of a fuel cell operating on H_2 and CO fuel gas and an oxidant of air. ⁷

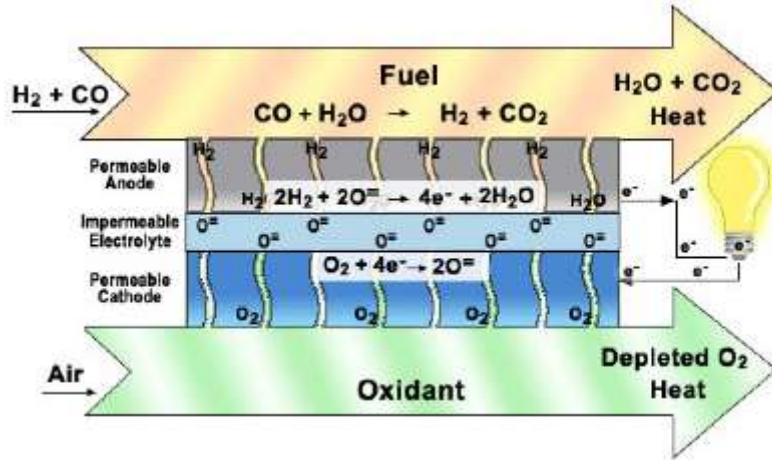


Figure 1. Schematic of a fuel cell operating on a H₂ and CO fuel gas and air as the oxidant.

1. Cathodes

The cathode of a SOFC needs to be: electrically conductive, an effective catalyst for the reduction of oxygen (Eq. 1), possess a continuous porous network for gas transport, nonreactive with other fuel cell materials at fabrication and operation temperatures, and have a CTE similar to the anode and electrolyte.



Platinum was the first cathode material used because of its high conductivity and activity for oxygen reduction. However, the high cost of platinum makes it impractical for large scale fuel cell production. Currently, the most commonly used material for cathodes is strontium doped lanthanum manganite (LSM).^{6,8}

2. Electrolytes

The purpose of the electrolyte in a SOFC is to allow the diffusion of oxygen ions from the cathode to the anode while providing an electrically insulating barrier between the anode and the cathode. Therefore, the electrolyte of SOFCs must be stable in both oxidizing and reducing atmospheres, have high ionic conduction at operating temperatures, and have little to no electronic conduction at operating temperatures. The most commonly used electrolyte for SOFCs is yttrium-stabilized zirconia (YSZ), however,

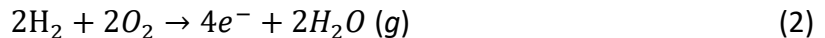
other materials, including but not limited to other doped zirconia and ceria materials, have been researched.⁹

3. Anodes

The anode of a SOFC should meet the following basic requirements: ^{1,3,10-12}

- High electro-catalytic activity for the oxidation of fuel gases
- High electrical conductivity for the movement of reaction electrons to the interconnect
- Possess a continuous porous structure to allow transport of fuel and reaction products to and from the triple phase boundary (TPB)
- Fuel flexible, low cost, and easy to fabricate
- TEC compatible with other SOFC components

As seen in Figure 1, the anode is where the fuel gas is oxidized by O⁻² ions which diffuse from the cathode through the electrolyte. The fuel oxidation reaction does not take place across the entire anode, but only in the region referred to as the triple phase boundary. For a fuel cell operating with a fuel gas of H₂ the hydrogen oxidation reaction (HOR) equation is:



When a fuel cell is operating on a mixture of CO and H₂ fuel the HOR has been the primary reaction that is considered because Holtappels et al.¹³ argued that most of the CO would participate in the water-gas shift reaction rather than in the electrochemical reaction since the electro-oxidation of H₂ proceeds 2-3 times faster than CO across Ni-YSZ.¹⁴ This was further supported when Weber et al.¹⁵ reported no significant difference in performance between a cell operating on pure H₂ and a cell with a gas mixture of 25% CO and 75% H₂. However, Ong et al.¹⁶ recently reported that CO electro-oxidation does play a role in SOFC performance, particularly at high anode overpotentials.

Nickel-based cermets are the standard commercial anodes because of their low cost, high electrical conductivity, and high activity for the reforming of hydrocarbon fuels.

However, Ni-based cermets are not without problems. It is well known that Ni-based cermets have problems such as Ni coarsening, low coking and sulfur poisoning resistance, and redox instability, all of which degrade performance and lead to failure of the SOFC.^{10,11,17-19}

Ni particle coarsening, agglomeration, and densification are the predominant microstructural changes of SOFC anodes operating at high temperatures. Ni coarsening causes a decrease in the number of catalytically active sites for the electro-oxidative HOR to occur. This decrease in active sites reduces the reaction rate, and therefore degrades fuel cell performance. Thermodynamically, there will always be a driving force to reduce the free energy of the system through coalescence of particles. Coupled with the low melting point of nickel and the non-wettability of Ni towards YSZ, these microstructural changes are unavoidable at high temperatures. However, Simwonis et al.²⁰ observed that nickel coarsening occurs relatively slowly during an experimental period of 4000 hours at 1000°C.

During long term operation, SOFCs experience multiple redox cycles. Based on the molar volumes of NiO and Ni, the oxidation of Ni is accompanied with an increase in solid volume by 69.9%. It was suggested that concurrent with the reduction of NiO, coalescing and sintering of Ni takes place, leading to a network of coarser Ni particles. Upon re-oxidation, the associated volume change of the coarser particles would generate enough stress to cause mechanical degradation via cracking.²¹

In an effort to improve SOFC anodes many alternative anode materials have been researched including fluorites, perovskites, double perovskites. However, due to the variability in research and the lack of reproduction of much of the work it is difficult to effectively compare the anodes. Table II gives a brief summary of the full cell configuration with peak power density, measurement temperature, and fuel gas for fuel cells materials that have been researched.

Table II. Summary of Potential Fuel Cell Materials with Operation Temperature and Associated Fuel Gas and Peak Power Densities

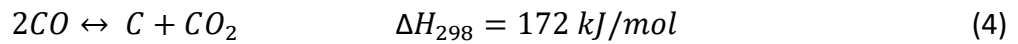
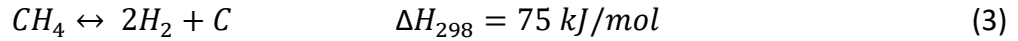
Anode	Electrolyte	Cathode	Temperature (°C)	Fuel Gas	Maximum Power Density (mW·cm ⁻²)	Reference
Ni-YSZ	YSZ	LSM-YDC	650	3% H ₂ O CH ₄	370	22 23
			600		250	
			550		130	
La _{0.75} Sr _{0.25} Cr _{0.5} Mn _{0.5} O ₃	YSZ (Al ₂ O ₃)	LSM	900	wet H ₂	470	24
			900	wet 5% H ₂	290	
			900	wet CH ₄	200	
			850	wet 5% H ₂	200	
La _{0.8} Sr _{0.2} Sc _{0.2} Mn _{0.3} O ₃	(Sc ₂ O ₃) _{0.1} (ZrO ₂) _{0.9}	La _{0.8} Sr _{0.2} Sc _{0.2} Mn _{0.3} O ₃	900	wet 3% H ₂ O H ₂	310	25
			900	wet 3% CH ₄	130	
			850	wet 3% H ₂ O H ₂	220	
			850	wet 3% CH ₄	100	
La _{0.8} Sr _{0.2} Cr _{0.5} Mn _{0.5} O ₃₋₆ +Cu+Pt	La _{0.8} Sr _{0.2} Ga _{0.83} Mg 0.17O _{2.185}	SrCo _{0.8} Fe _{0.2} O ₃₋₆	850	dry H ₂	850	26
			800	dry H ₂	500	
			850	CH ₄	520	
			800	CH ₄	450	
La _{0.8} Sr _{0.2} Cr _{0.5} Mn _{0.5} O ₃₋₆ porous	La _{0.8} Sr _{0.2} Ga _{0.83} Mg _{0.17} O _{2.185}	SrCo _{0.8} Fe _{0.2} O ₃₋₆	800	H ₂	175	
			850	CH ₄	250	
La ₄ Sr ₈ Ti ₁₁ Mn _{0.5} Ga _{0.5} O ₃₈₋₆	YSZ	LSM	950	97.7% H ₂ / 2.3% H ₂ O	500	27
			950	97.7% CH ₄ / 2.3% H ₂ O	350	
			950	5% H ₂	170	

Anode	Electrolyte	Cathode	Temperature (°C)	Fuel Gas	Maximum Power Density (mW·cm ⁻²)	Reference
Sr ₂ MgMoO ₆₋₆	LSGM (with a LCD buffer layer)	SrCo _{0.8} Fe _{0.2} O ₃₋₆	850	H ₂	968	28,29
			800	H ₂	838	
			750	H ₂	642	
			800	dry CH ₄	438	
			800		338	
			800	H ₂ / H ₂ S	829	
			800	H ₂ / H ₂ S -3% H ₂ O	800	
			800	97% H ₂ / 3% H ₂ O	811	
Sr ₂ MnMoO ₆₋₆	LSGM (with a LCD buffer layer)	SrCo _{0.8} Fe _{0.2} O ₃₋₆	800	H ₂	658	
			750	H ₂	467	
			800	dry CH ₄	118	
La _{0.8} Sr _{0.2} Cr _{0.82} Ru _{0.18} O ₃₋₆ - Ce _{0.9} Gd _{0.1} O _{1.95}	La _{0.9} Sr _{0.1} Ga _{0.8} Mg _{0.2} O ₃₋₆	La _{0.6} Sr _{0.4} Co _{0.2} Fe _{0.8} O ₃₋₆ -GDC	800	wet H ₂	390	30
Gd ₂ Ti _{1.4} Mo _{0.6} O ₇	YSZ	La _{0.75} Sr _{0.25} Cr _{0.5} Mn _{0.5} O ₃	850	10% H ₂ S - H ₂	140	31
La _{0.3} Sr _{0.7} TiO ₃ - YSZ	YSZ	LSM - YSZ	850	wet H ₂	15	32
La _{0.3} Sr _{0.7} Ti _{0.8} Cr _{0.2} O ₃ - YSZ	YSZ	LSM - YSZ	850	wet H ₂	25	
La _{0.4} Sr _{0.5} Ba _{0.1} TiO ₃ - YSZ	YSZ	LSM- YSZ	800	0.5% H ₂ S/ dry CH ₄	50	33
La _{0.6} Sr _{0.3} Cr _{0.85} Ni _{0.15} O ₃ -YSZ	YSZ	YSZ-LSM	800	H ₂	309	34
				5000 ppm H ₂ S - H ₂	460	
La _{0.7} Sr _{0.3} Cr _{0.85} Ni _{0.15} O ₃ - YSZ	YSZ	YSZ-LSM	800	H ₂	78	
				5000 ppm H ₂ S - H ₂	135	
La _{0.6} Sr _{0.3} Cr _{0.85} Fe _{0.15} O ₃ -YSZ	YSZ	YSZ-LSM	800	5000 ppm H ₂ S - H ₂	365	
La _{0.6} Sr _{0.3} Cr _{0.85} Co _{0.15} O ₃ - YSZ	YSZ	YSZ-LSM	800	5000 ppm H ₂ S - H ₂	345	
La _{0.9} Ca _{0.1} Fe _{0.9} Nb _{0.1} O ₃₋₆ - ScSz	ScSz	LSF-ScSZ	750	H ₂	467	35

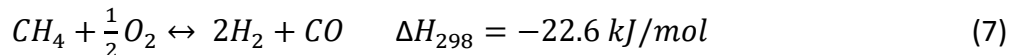
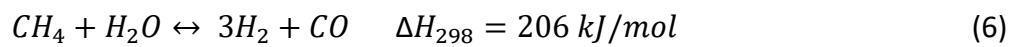
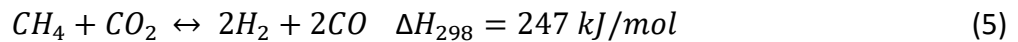
Anode	Electrolyte	Cathode	Temperature (°C)	Fuel Gas	Maximum Power Density (mW·cm ⁻²)	Reference
			750	CO	376	
La _{0.9} Ca _{0.1} Fe _{0.95} Nb _{0.05} O ₃₋₆ - ScSZ	ScSZ	LSF-ScSZ	750	H ₂	463	
Cu-CeO ₂ -YSZ	YSZ	YSZ-LSM	800	H ₂	310	³⁶
			800	n-butane	180	
			700	H ₂	220	
			700	n-butane	120	
Ru-CeO ₂ /Ni-YSZ	YSZ	LSCF-GDC	770	5% iso-octane/9% air/ 86% CO ₂	650	³⁷
			720		500	
			670		350	
			620		200	
			570		100	

C. Carbon Deposition

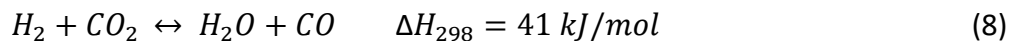
One of the primary benefits of SOFCs over other fuel cell technologies is the high operating temperature which enables fuels to be internally reformed on the anode. Unfortunately, the internal reforming of hydrocarbons across Ni-YSZ cermet anodes is often accompanied by carbon deposition. Carbon deposition, often referred to as “coking” or “carburization”, takes place through the catalytic dissociative adsorption of hydrocarbons on the surface of Ni. With alkane based fuels such as methane, carbon formation occurs through methane dissociation (Eq. 3) or CO disproportionation also known as the Boudouard reaction (Eq. 4).³⁸



The addition of steam, carbon dioxide, or oxygen to fuel gases is a common technique used to suppress carbon formation. The reforming of methane in a SOFC can be described through three main reactions: methane dry reforming (MDR) (Eq. 5), methane steam reforming (MSR) (Eq. 6), and partial oxidation with air (MPO) (Eq. 7)³⁹



However, the water-gas shift reaction (Eq. 8) must also be considered because of its effects on CO: H₂ production.^{19,39}



Carbon deposition deactivates the electrochemically active sites of the anode, resulting in a loss of the fuel cell's performance. Carbon can form a wide range of structures including adsorbed, polymeric, vermicular filaments, carbide, and graphitic.

Each structure has a different activity for reacting with Ni, and thus affects the deactivation of the catalytic sites in different ways.¹⁷

The likelihood of carbon deposition can be estimated by the oxygen: carbon (O:C) and the hydrogen: carbon (H:C) ratios in the feed gas.⁴⁰ A low ratio for both O:C and H:C will favor the tendency towards carbon deposition. Therefore, carbon deposition is favored in dry reforming methane when the CH₄:CO₂ ratio is 1:1 which correlate to an O:C=1 and an H:C=2. In comparison, it has been reported that steam reforming with 1 CH₄:1 H₂O does not have as high a tendency for carbon deposition because of an associated H:C=6 and O:C=1.⁴⁰ However, due to the large quantity of steam that is required for SRM, with heavier hydrocarbons requiring more steam, it is not entirely practical.⁴¹ The large amount of steam that is necessary for steam reforming decreases the fuel cell efficiency because of fuel dilution and the increase of pO₂ in fuels which decreases the open cell voltage. Furthermore, excess steam can induce thermal stress that could damage fuel cell components.^{19,42} Coking is less problematic in intermediate temperature SOFCs (IT-SOFCs) since they operate at temperatures below some of the thermally activated reactions.

A large amount of research has been done attempting to improve SOFC anodes resistance to coking and sulfur poisoning. Guerra et al.⁴³ researched optimal operating parameters of SOFC such as temperature, gas residence time, and inlet CO₂:CH₄ ratios⁴³ to avoid carbon deposition. Other authors have studied alternative anode materials such as those reported in Table II. However, no alternative materials that have been developed have displaced Ni cermets as the industrial standard. Therefore, there have been a rising number of researchers that are adding an internal reforming layer to Ni based anodes.⁴⁴⁻⁴⁸ The internal reforming layer should provide a protective barrier between the hydrocarbon fuels and the anode by reforming the hydrocarbons into H₂ and CO prior to contact with the anode itself.

Several authors have demonstrated increased performance and fuel cell stability when utilizing an internal reforming layer. Jin et al.⁴⁴ reported stable performance while operating at 650°C in methane for 60 hours with a Cu_{1.3}Mn_{1.7}O₄ spinel internal reforming

layer on a Ni-scandium doped ceria (SDC) anode. The same authors reported a maximum power density improvement of approximately 30% when operating under a methane atmosphere at 650°C and 700°C compared to the fuel cells that did not have the internal reforming layer. Furthermore, Wang et al. ⁴⁹ applied a Ni/Al₂O₃ reforming layer to a Ni-ScSZ cermet anode and observed a power density increase to almost double that of a cell without the functional layer while operating on methane at 750°C and 850°C. The increase in power density was attributed to the functional layer acting as a diffusion barrier to reduce the concentration of methane within the anode. The diffusion barrier also reformed methane prior to it contacting the anode, which decreased the formation of carbon on the anode via methane cracking.

D. SOFC Power Measurements

The most commonly reported metrics for SOFCs are the power density versus current density and current density versus voltage. The power density of a fuel cell is measured by applying a stimulus current and recording the corresponding voltage. Power density is defined by the following equation:

$$P_{dens} = VJ \quad (9)$$

where P_{dens} is the power density in $W \cdot cm^{-2}$, V is the voltage in V, and J is the current density in $A \cdot cm^{-2}$.

Current density (J) of a fuel cell is defined as the current (I) divided by the active area of the fuel cell. The current, I , is a linear function of the molar flow of the electrons or molar flow of the spent fuel.

The open cell voltage of an ideal fuel cell is independent of current density because the flow rates of fuel and oxidant are sufficiently high such that the fuel and oxidant compositions just outside of the anode and cathode are virtually fixed. However, this is not the case in a real fuel cell. In actual systems, the voltage is a function of the current density. Furthermore, voltage is also decreased by polarization that occurs in the fuel cell due to imperfections in the materials, microstructure, and design of the SOFC.

Polarization can be broken down into ohmic polarization, concentration polarization, and activation polarization.

1. Ohmic Polarization

With the exception of superconductors, all matter has a resistance to the motion of electrical charge. In a fuel cell, there are two charge carriers that are moving throughout the SOFC: ions moving across the electrolyte and electrons moving across the electrodes. In the simplest of cases, this relationship can be described through Ohm's law. The dominant ohmic losses, through the electrolyte, can be reduced by decreasing the distance of electrode separation and enhancing the ionic conductivity of the electrolyte.

2. Concentration Polarization

Concentration polarization is caused by the transportation of gaseous reactants and products throughout the anodes and cathodes. This transport must be consistent with the net current flowing through the cell. The physical "resistance" to the transport of the gaseous species through the anode at a given current density causes an electrical polarization. The concentration polarization is a function of diffusivity of the reactants and products, microstructure of the anode, partial pressures, and current density. Concentration polarization increases with increasing current density, but it is not a linear relationship.

3. Activation Polarization

Kinetically, all chemical reactions, including electrochemical reactions, involve energy barriers which must be overcome by the reacting species. This energy barrier, referred to as the 'activation energy,' results in activation or charge-transfer polarization, which is caused by the transfer of charges between the electronic and the ionic conductors. The activation polarization may be regarded as the extra potential necessary to overcome the energy barrier of the rate-determining step of the reaction to a value such that the electrode reaction occurs at a desired rate. ^{11,50,51}

E. Spinel Catalysts

Normal spinel materials have been widely studied by catalyst researchers for their use as a reforming catalyst for H_2 production.^{40,52-55} Spinel type materials have a formula of AB_2O_4 , with A being a divalent cation on a tetrahedral site and B being a trivalent cation located on an octahedral site. (Figure 2)

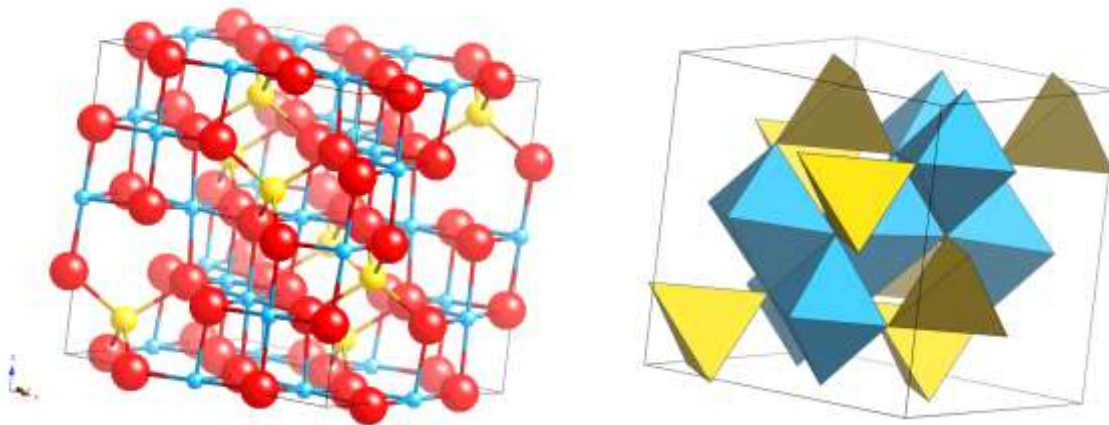


Figure 2. A representation of the spinel structure rendered using CrystalMaker software; yellow atoms occupy the A site, blue atoms occupy the B site, and red atoms represent oxygen.

When under a reducing atmosphere, with sufficient time and temperature, the element that occupies the A site of the spinel can be reduced out of the matrix to form nanoparticles on the spinel surface. It has been reported that the formation of carbon hindered by decreasing the catalyst particle size and also having a strong interaction between the metal particles and the support.⁴⁰ Therefore, spinel materials, which are able to reduce out catalytically active A site nanoparticles from the bulk spinel, are one of the structures that have been researched for coking-resistant reforming catalysts. Hill et al.⁵⁶ reported that during the reduction process of $Ni_xMg_{1-x}Al_2O_4$, one O^{2-} was lost from the spinel for each Ni^{2+} reduced to Ni metal. This yields $MgAl_2O_4$ spinel support with well dispersed Ni nanoparticles on the spinel surface. In addition, spinel materials have also been recognized as being able to be regenerated to their original reforming performance through redox cycling, if the nanoparticles are coked or poisoned.^{57,58}

Previous work at Alfred University has shown that $\text{Ni}_{0.375}\text{Co}_{0.375}\text{Mg}_{0.25}\text{Al}_2\text{O}_4$ and $\text{Ni}_{0.375}\text{Cu}_{0.375}\text{Mg}_{0.25}\text{Al}_2\text{O}_4$ spinels are stable catalysts for methane dry reforming.⁵⁷ Under reducing conditions, the spinels are able to reduce out catalytically active Ni-Cu and Ni-Co alloy nanoparticles on top of a MgAl_2O_4 support. These nanoparticles are characterized by their high reforming activity due to the nickel and also exhibits an increased resistance to carbon deactivation because of the copper or cobalt. Furthermore, the nanoparticles, which will undergo particle growth, poisoning by sulfur, and deactivation due to coking, can be oxidized, absorbed back into the spinel support, and reduced out again to regenerate the catalyst. In the present work, $\text{Ni}_{0.375}\text{Cu}_{0.375}\text{Mg}_{0.25}\text{Al}_2\text{O}_4$ will be investigated for its potential use as an internal reforming layer for a Ni-YSZ SOFC anode.

EXPERIMENTAL PROCEDURE

A. Powder Synthesis

Solid state synthesis was used to produce $\text{Ni}_{0.375}\text{Cu}_{0.375}\text{Mg}_{0.25}\text{Al}_2\text{O}_4$. NiO (97%, Fisher Scientific), Co_3O_4 (99.7%, Alfa Aesar), anhydrous Al_2O_3 (99%, Fisher Scientific), and Cu_2O (99.95%, Alfa Products) were used as reactants. The loss on ignition (LOI) of each of the precursors was measured and accounted for in calculations. Stoichiometric amounts of the powders were weighed and mixed in a suspension of deionized water with a McCrone Micronizing Vibratory Mill. The suspension was milled in a plastic jar with alumina milling media for 10 minutes. After milling, the suspension was dried on a hot plate and agglomerates were broken up via mortar and pestle. The dried powder was then pressed into pellets at a pressure of 5 metric tons and calcined at 1500°C in a molybdenum disilicide furnace for 16 hours with a heating and cooling rate of $5\text{K}/\text{min}$. An intermediate grinding in an alumina mortar and pestle were completed at 8 hours. After grinding, the powder was pressed into pellets again and placed back into the furnace. X-ray powder diffraction was performed using a Bruker D8 Advance Diffractometer with $\text{Cu-K}\alpha$ radiation to ensure phase purity. The XRD pattern for the prepared spinel can be found in Appendix A.

B. Room Temperature X-ray Diffraction

X-ray diffraction patterns were collected using a Bruker D8 Advance Diffractometer with $\text{Cu-K}\alpha$ radiation, a 2.5° Soller slit, a 15 mm incident beam slit, 30 rotations per minute in-plane spinning, a Ni filter $\text{K}\beta$ filter, and a LynxEye position sensitive detector. Furthermore, the XRD patterns were measured from $15^\circ 2\theta$ to $70^\circ 2\theta$.

C. High Temperature X-ray Diffraction Measurements for Coefficient of Thermal Expansion (CTE)

For high temperature measurements X-ray diffraction patterns were collected using a Bruker D8 Advance Diffractometer with $\text{Cu-K}\alpha$ radiation. The sample was heated from room temperature to 850°C with a heating rate of 30°C per minute and the diffraction patterns, from $15^\circ 2\theta$ to $70^\circ 2\theta$, were collected every 50K on cooling. The resulting diffraction patterns were analyzed using Bruker's TOPAS™ XRD software.

Rietveld refinements were used to calculate the lattice parameters of the spinel for each temperature and the coefficient of thermal expansion was calculated from the lattice parameter changes.

D. Phase Interaction Study

$\text{Ni}_{0.375}\text{Cu}_{0.375}\text{Mg}_{0.25}\text{Al}_2\text{O}_4$ (Cu375), NiO, and YSZ or GDC in a 1:1:1 weight percent ratio were mixed by vibratory mill, dried, and pressed into pellets. The pellets were then fired in air at 1300°C, 1400°C, or 1500°C with a heating and cooling rate of 5K/minute and a dwell time of 6 hours. After firing, the pellets were ground using an alumina mortar and pestle and X-ray powder diffraction was completed to determine the phases present.

E. Fuel Cell Preparation

Nextcell 2.0 button cells were purchased from Fuel Cell Materials¹. The button cells consisted of a ~50 μm thick NiO-YSZ anode electrode, a 0.13-0.17 mm thick Hionic™ electrolyte support, and a ~50 μm thick LSM/LSM-GDC cathode electrolyte. Two methods were used to deposit the spinel on the surface of the anode. For partial coverage of the spinel, 0.15 g of spinel was suspended in 5mL of isopropanol (3 wt.%). The suspension was shaken vigorously by hand before pipetting 0.5mL of the suspension from the test tube and dripping it onto the anode. For complete coverage of spinel on the anode, a sedimentation method was employed. A 5 wt.% suspension of spinel in DI water was batched and 1 mL of the suspension was pipetted from the test tube onto the surface of the anode. The suspension was contained by using a tube with a diameter of 15 mm around the anode. The fuel cell with surface suspension was air dried for 2 hours and then placed in a drying oven at 100°C for 5 hours.

F. Electrochemical Performance

¹ <https://fuelcellmaterials.com/products/cells/nextcell-electrolyte-supported-button-cell/>

Electrochemical performance measurements were completed using a Norwegian Electro Ceramics AS Probostat™ fuel cell testing assembly (Figure 3).

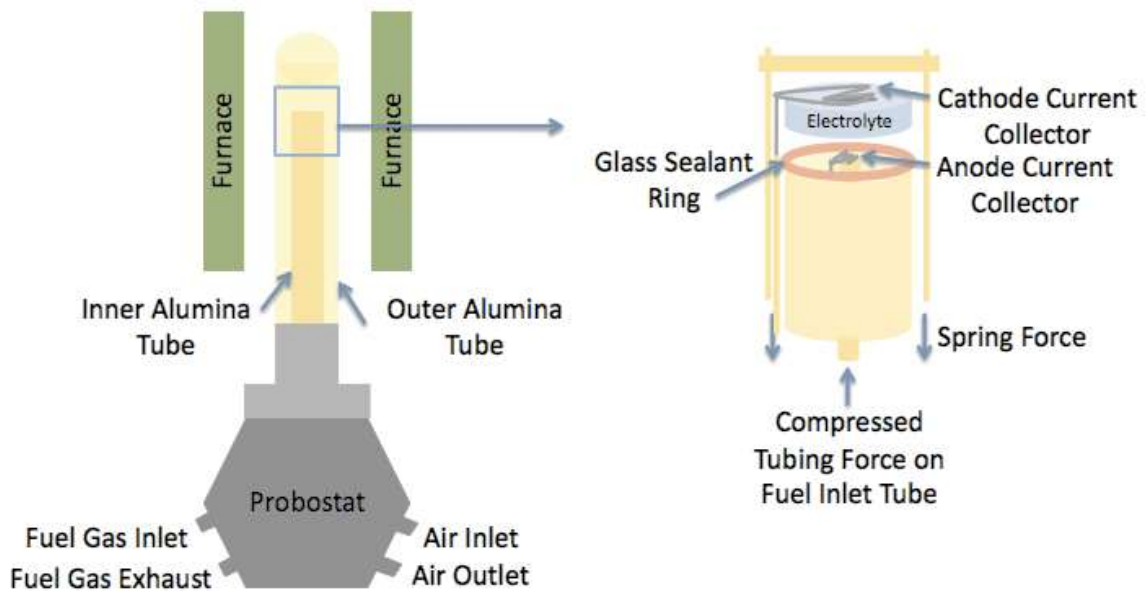


Figure 3. Schematic of Probostat™ fuel cell testing apparatus (left) with enlarged fuel cell and current collector diagram (right).

The volume of the outer alumina tube is approximately 715 cm³ and the volume of the inner alumina tube is approximately 98 cm³. The button cell was sealed onto the inner alumina tube using a gallio-boro-silicate glass (specifically GaBA4⁵⁹), and platinum mesh current collectors were used on the anode and cathode. A BK Precision 300W Programmable DC Electronic Load Model 8500 was used as a stimulus and response detection system. Constant current was applied to the fuel cell, and the responsive voltage was measured.

The fuel cell testing module was heated to 900°C at a rate of 10K/minute. Once at temperature, the anode of the fuel cell was reduced for 3 hours using flowing 4% H₂ and 96% N₂ at a flow rate of 100 standard cubic centimeters per minute (scm). Compressed air was fed to the cathode at a rate of 180 sccm. After 3 hours, the sample was cooled to either 850°C, 750°C, or 650°C and voltage and responsive currents or

currents and responsive voltage were collected. Fuel gases that were used were 4% H₂ - 96% N₂, 32% CH₄ – 63% CO₂ – 5% N₂, or 47.5% CH₄ – 47.5% CO₂ – 5% N₂.

For fuel cell endurance testing 47.5% CH₄ – 47.5% CO₂ – 5% N₂ was fed to the fuel cells at a constant rate of 70 sccm, and the fuel cells were kept at a constant temperature of 850°C. Between I-V measurements, a constant current of 0.133 amps was applied to the fuel cell. The measurements were conducted for a minimum of 52 hours.

G. Scanning Electron Microscopy

After electrochemical performance measurements, the button cells were imaged using a FEI Quanta 200F Environmental Scanning Electron Microscope equipped with an EDAX Energy Dispersive Spectroscopy system. If needed, samples were coated with a gold-palladium coating applied via sputter coating. After fuel cell endurance testing, an accelerating voltage of 5eV was used to image the fuel cells.

H. Raman Spectroscopy

Raman shift measurements were completed to identify the type of carbon that was present on the fuel cell anodes after endurance testing. Raman shift measurements were completed at Cornell University using a Renishaw inVia confocal Raman microscope with a 488 nm laser. The Raman spectra were analyzed using Renishaw WiRE™ 4 software. Previous work at Alfred University with Ni_{0.375}Cu_{0.375}Mg_{0.25}Al₂O₄ operating under dry reforming conditions showed that graphitic carbon, with peaks at 1350 cm⁻¹ (D band) and 1585 cm⁻¹ (G band), was the primary form of carbon deposition on the spinel after 12 hours on stream of catalysis testing.⁵⁷

RESULTS

A. Phase Compatibility

1. $\text{Ni}_{0.375}\text{Cu}_{0.375}\text{Mg}_{0.25}\text{Al}_2\text{O}_4$ - NiO - YSZ

To determine if the spinel would react with the anode during fabrication of the fuel cell, powders of NiO-YSZ- $\text{Ni}_{0.375}\text{Cu}_{0.375}\text{Mg}_{0.25}\text{Al}_2\text{O}_4$ (Cu375) and NiO-GDC-Cu375 were thoroughly mixed, pressed into pellets, and heat treated. The XRD patterns for the NiO-YSZ-Cu375 mixture after heat treatments can be seen in Figure 4. As the heat treatment temperature increases there is an accompanying increase in spinel peak relative intensity and a decrease in NiO peak relative intensity. The change in relative intensities for NiO and spinel are also accompanied by spinel peaks shifting slightly towards a higher nickel concentration spinel, indicating the spinel is reacting with the excess nickel to form additional spinel. Furthermore, a shift in the YSZ peaks was observed. Rietveld refinement of the XRD patterns revealed a decrease in the a lattice parameter of ~ 0.02 angstroms when fired with NiO and spinel.

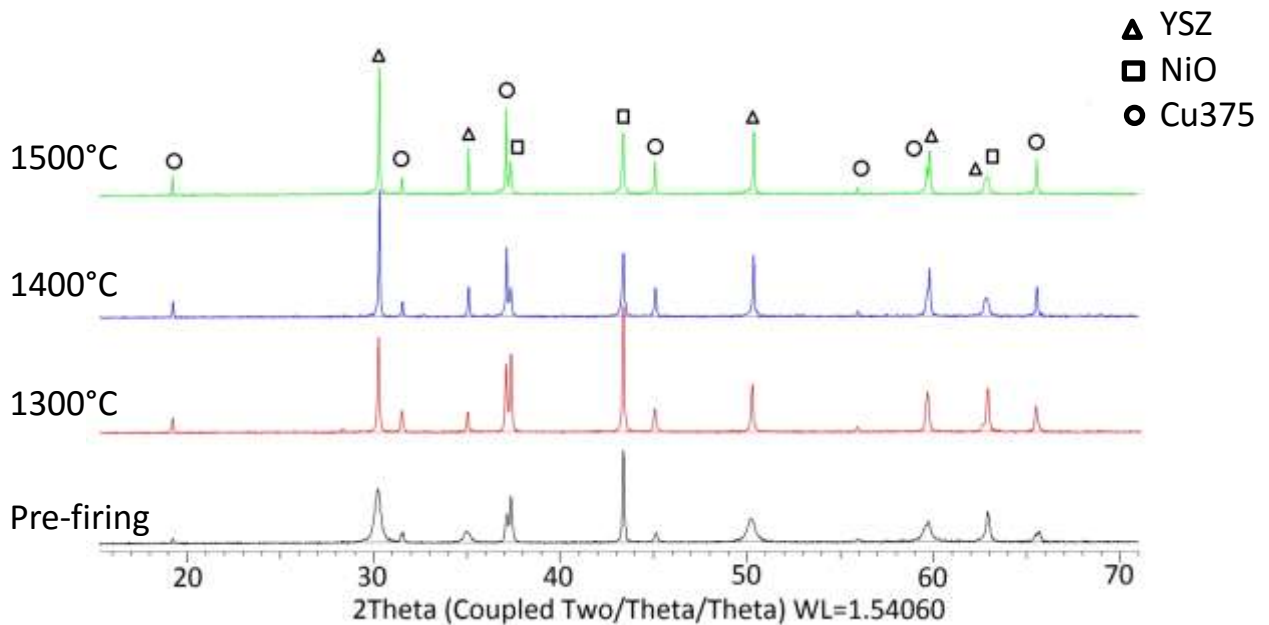


Figure 4. XRD patterns for phase compatibility study of NiO-YSZ-Cu375. Spinel peak intensity increases while NiO peak intensity decreases, most obviously at 37° 2 θ (Cu375) and 37.3° 2 θ (NiO).

2. $\text{Ni}_{0.375}\text{Cu}_{0.375}\text{Mg}_{0.25}\text{Al}_2\text{O}_4$ - NiO - GDC

The resulting XRD patterns from the NiO-GDC-Cu375 phase compatibility study can be seen in Figure 5. Similar to the previous results, as temperature increases NiO peak relative intensity decreases as the spinel composition changes towards a higher Ni concentration spinel. The spinel composition change causes the peaks to shift. There were no observable changes to the GDC phase.

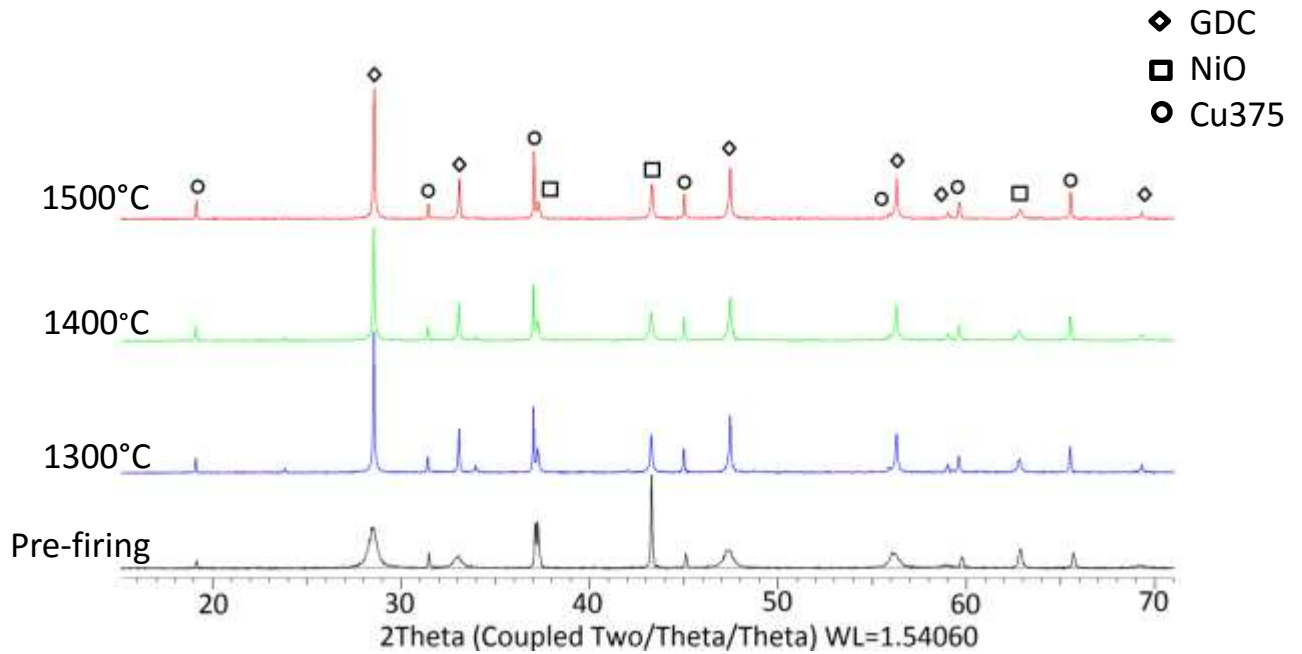


Figure 5. XRD patterns for NiO-GDC-Cu375 phase compatibility study. The spinel peaks show an increase in intensity as temperature increases concurrently with a decrease in intensity of the NiO peaks.

B. Coefficient of Thermal Expansion

The coefficient of thermal expansion of the spinel from room temperature to 850°C was calculated using the HTXRD data. Through Rietveld refinements, the a lattice parameter for the spinel was determined for each pattern and plotted versus temperature. (Figure 6) The CTE of the oxide spinel was calculated to be $10 \times 10^{-6} \text{ K}^{-1}$ from 25°C to 850°C. The CTE of the spinel compared to YSZ, Ni, and Ni-YSZ cermets can be seen in Table III. The associated error from the Rietveld refinement can be found in Appendix B.

Table III. CTE of Fuel Cell Materials From 25°C to 1000°C and the Calculated CTE of Spinel From 25°C to 850°C

Material	CTE (10^{-6} K^{-1})
Ni	16.5 ⁶⁰
8 YSZ	10.5 ⁶⁰
$\text{La}_{0.8}\text{Sr}_{0.2}\text{MnO}_3$	11.7 ⁶⁰
$\text{Ni}_{0.375}\text{Cu}_{0.375}\text{Mg}_{0.25}\text{Al}_2\text{O}_4$ (oxide)	10.0

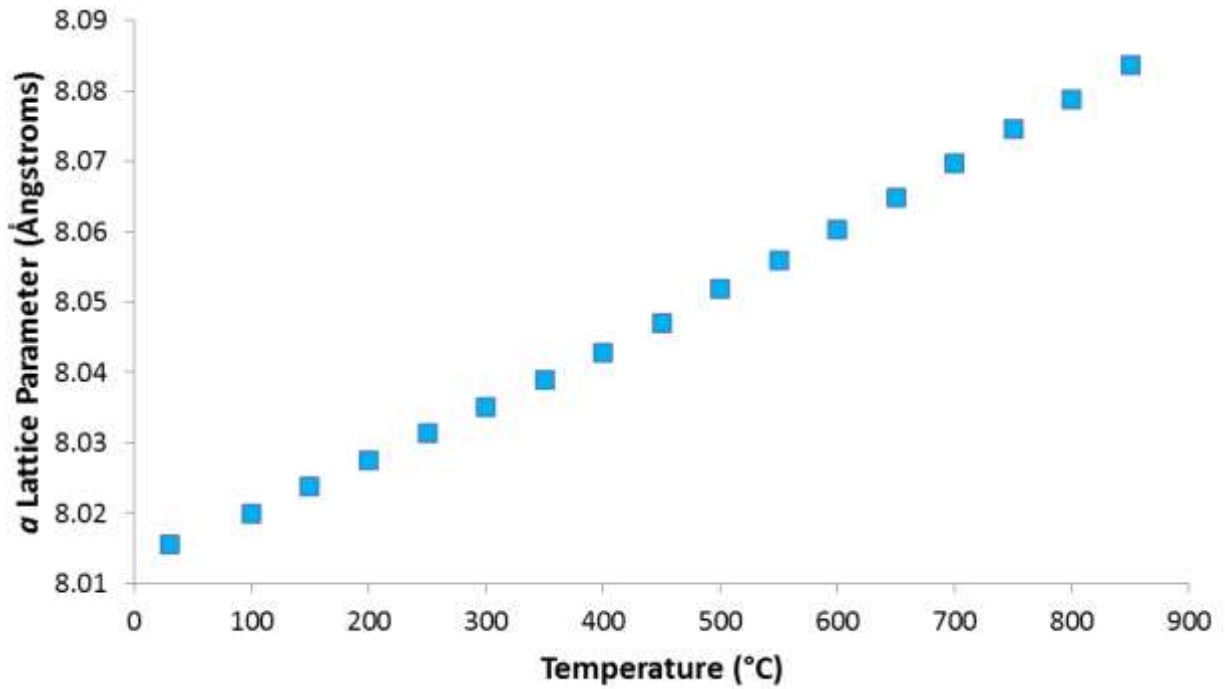


Figure 6. Lattice parameter vs temperature for $\text{Ni}_{0.375}\text{Cu}_{0.375}\text{Mg}_{0.25}\text{Al}_2\text{O}_4$.

C. Electrochemical Performance

When 0.015 g of spinel was added to the fuel cell anode, there was almost no change in the current density vs voltage and current density vs power density measurements which can be seen in Figure 7. The maximum power densities of the fuel cell with spinel were $0.070 \text{ W}\cdot\text{cm}^{-2}$, $0.052 \text{ W}\cdot\text{cm}^{-2}$, and $0.028 \text{ W}\cdot\text{cm}^{-2}$ at 850°C , 750°C , and 650°C , respectively. In comparison, the maximum power density of the fuel cell with no spinel additions was $0.069 \text{ W}\cdot\text{cm}^{-2}$, $0.049 \text{ W}\cdot\text{cm}^{-2}$, and $0.029 \text{ W}\cdot\text{cm}^{-2}$. While operating under H_2 the power density should not have changed significantly because the H_2 does not need to be reformed by the spinel catalyst. If a change were to occur, a decrease in the power density would be expected because the spinel has a lower electrical conductivity than the Ni-YSZ cermet. However, as discussed in depth later, the power density was similar between the samples because the platinum interconnect was able to contact the more electrically conductive Ni-YSZ cermet.

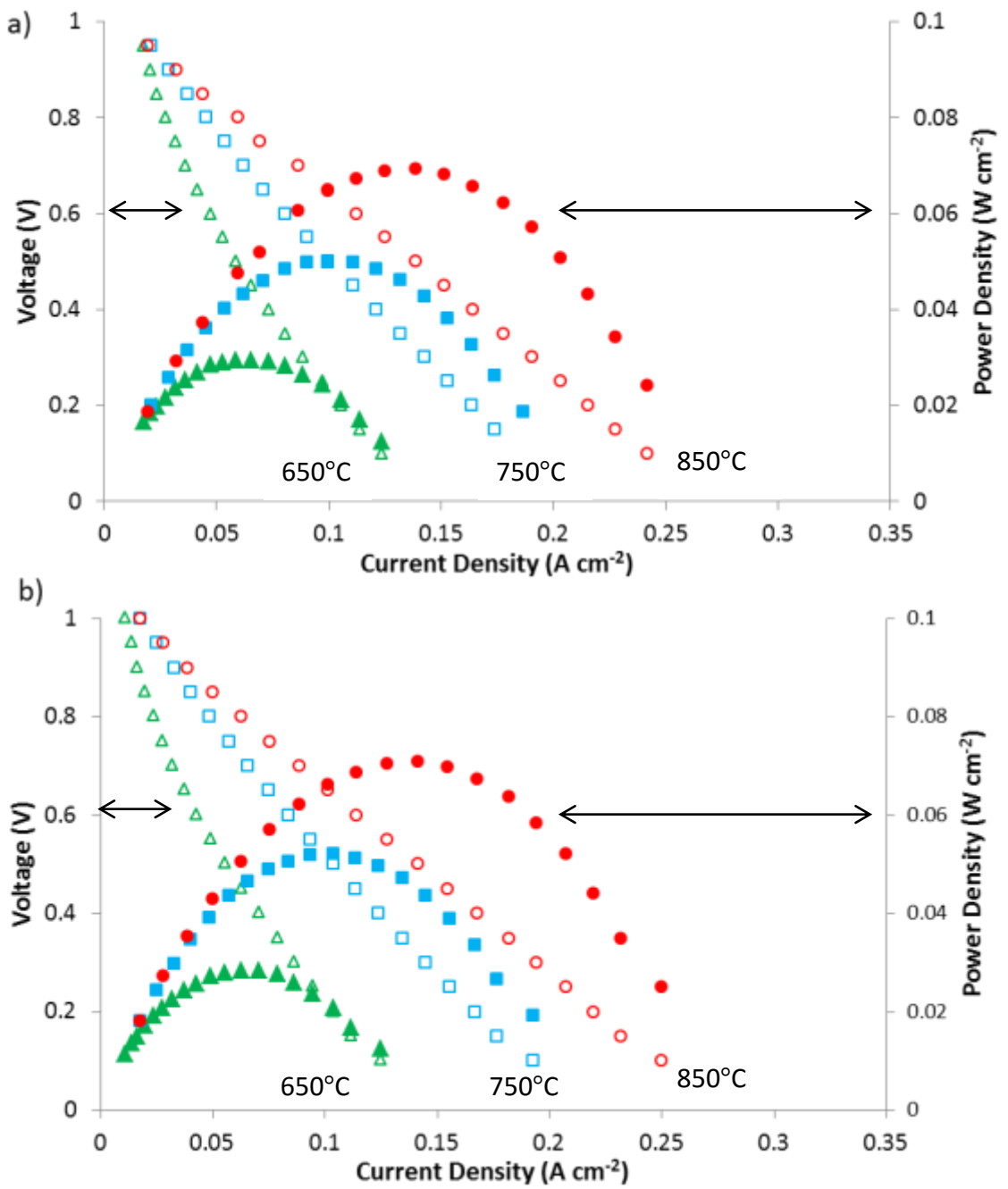


Figure 7. Current density vs voltage and current density vs power density curves of fuel cells (a) with spinel and (b) without spinel added on to anode.

When the same amount (0.015g) of spinel was added to a fuel cell that was operated in a 32% CH₄ – 63% CO₂ – 5% N₂ fuel gas mixture, the addition of the spinel caused an increase in the power density at both 850°C and 750°C as seen in Figure 8. The recorded maximum power density for the fuel cell with 0.015 g of spinel added was 0.098 W·cm⁻² at 850°C and 0.056 W·cm⁻² at 750°C. The measured maximum power density of the fuel cell with no spinel additions while operating with the 1:2 CH₄:CO₂ gas mixture was 0.074 W·cm⁻² at 850°C, and 0.040 W·cm⁻² at 750°C. The increase in power density was attributed to the spinel increasing the CH₄ and CO₂ reforming rate, while the anode was able to conduct charge efficiently through contact between the Ni-YSZ cermet and the interconnect. The addition of spinel increased the rate of methane reforming and increased the power density of the fuel cell by about 30% at both 750 and 850°C.

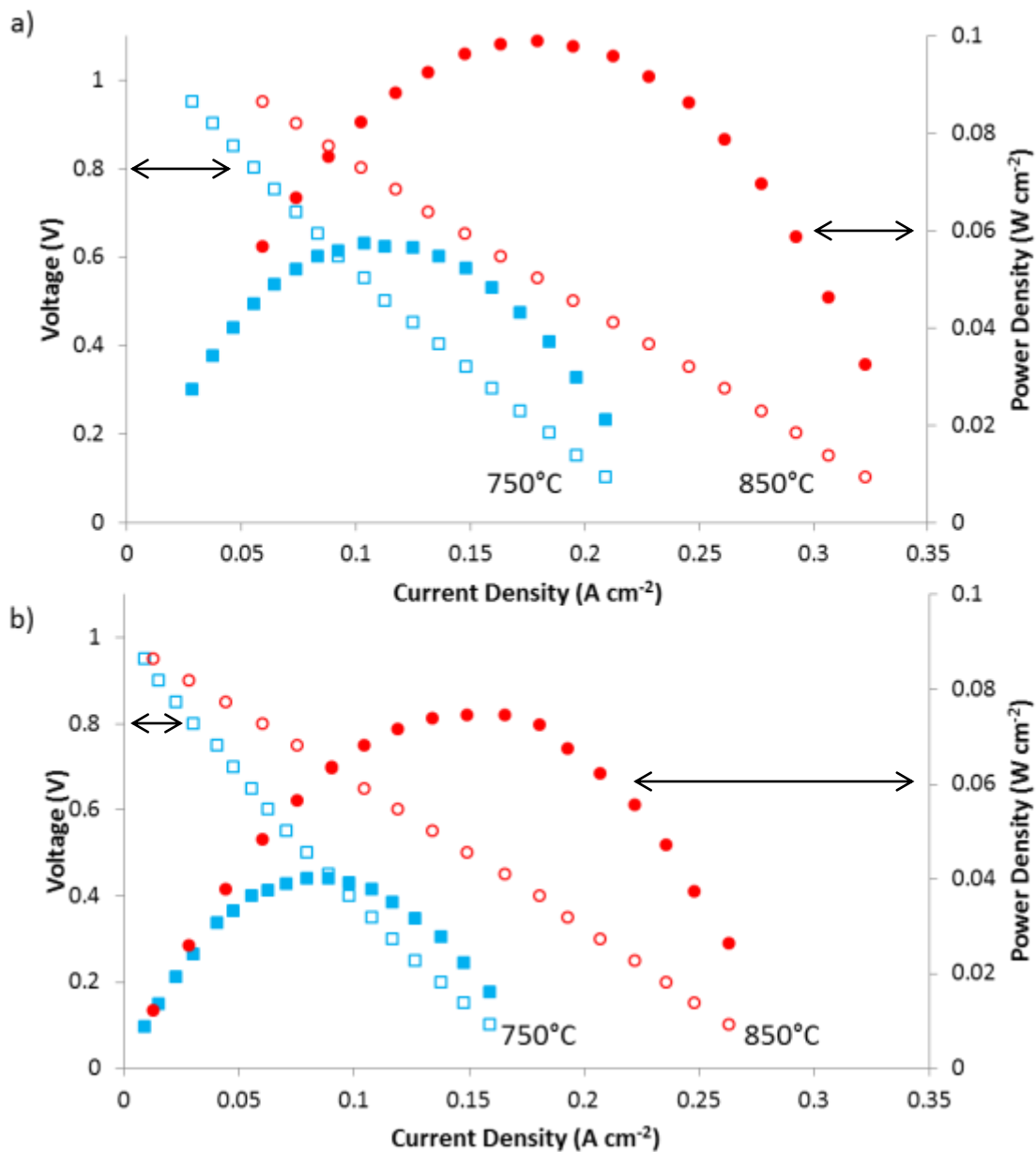


Figure 8. Current density vs voltage and current density vs power density curves for a fuel cell (a) with 0.015g of spinel added and (b) without spinel added operating under 32% CH₄ - 63% CO₂ - 5% N₂.

Figure 9 shows the maximum power density at 850°C compared to the time on stream for three samples: a fuel cell with 0.015g of spinel on the anode, a fuel cell with 0.05 g of spinel added, and a fuel cell with no spinel. The feed gas for all three samples was a coking mixture of 47.5% CH₄ - 47.5% CO₂ - 5% N₂. The fuel cell with 0.015 g of spinel

had a maximum power density of $0.116 \text{ W}\cdot\text{cm}^{-2}$ at 24 hours on stream. After 96 hours on stream the peak power density dropped by approximately 15% to $0.099 \text{ W}\cdot\text{cm}^{-2}$. The fuel cell that had 0.05 g of spinel added to the anode showed a 5% drop in maximum power density, from $0.084 \text{ W}\cdot\text{cm}^{-2}$ to $0.080 \text{ W}\cdot\text{cm}^{-2}$, after 56 hours on stream. Finally, without any spinel additions, the fuel cells were able to produce a maximum power density of $0.091 \text{ W}\cdot\text{cm}^{-2}$, which decreased about 15% after 52 hours to $0.077 \text{ W}\cdot\text{cm}^{-2}$. As discussed in more detail in the Discussion section, the primary difference in power density between the 0.015 g sample and the 0.05g sample was caused by the reduction in electrical conductivity of the anode. When 0.015 g of spinel was added to the fuel cell, the anode was not completely covered. The incomplete coverage allowed the platinum interconnect to contact the more electrically conductive Ni-YSZ. This, coupled with the postulated increased reforming rate from the spinel, increased the power density of the fuel cell. When 0.05 g of spinel was added to the fuel cell, the interconnect was in contact with the more insulating spinel which increased the ohmic resistance of the anode, and thus decreased the measured power density of the cell.

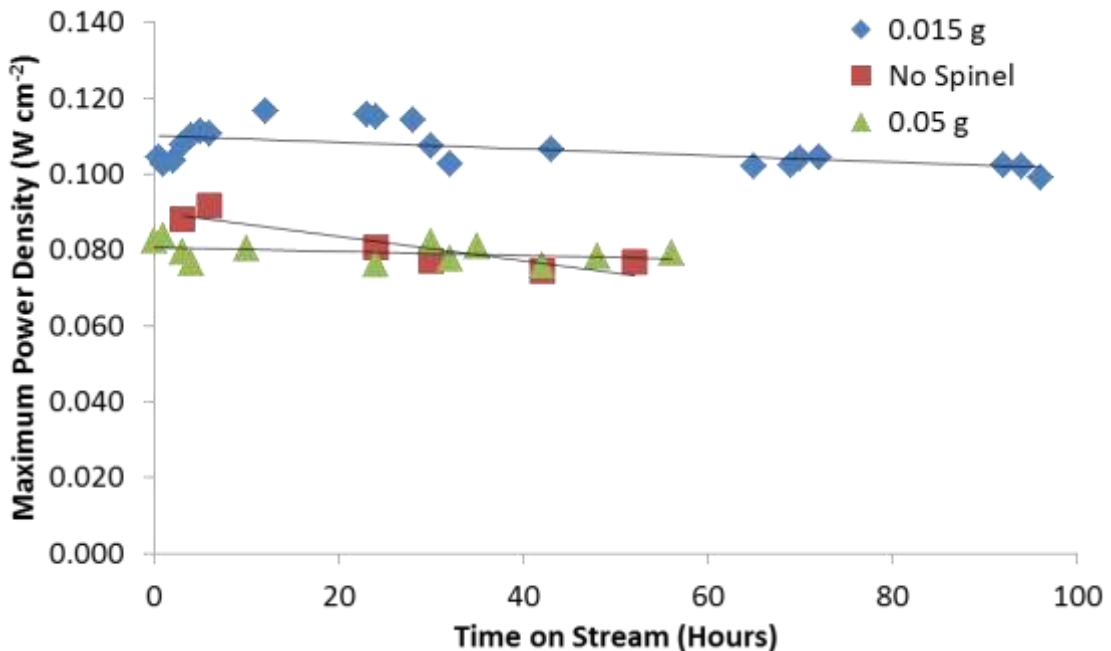


Figure 9. Maximum power density at 850°C of a fuel cell with 0.015g of spinel added, a fuel cell with 0.05g of spinel added, and a fuel cell with no spinel addition.

D. Scanning Electron Microscopy

1. Fuel Cell With No Spinel Additions

After 52 hours on stream under the 47.5% CH₄ - 47.5% CO₂ - 5% N₂ gas mixture no carbon fibers were apparent on the surface of the anode when observed using the scanning electron microscope as seen in Figure 10. As seen in the image, the anode is porous to permit transport of fuel to and from the triple phase boundary for electrochemical oxidation.

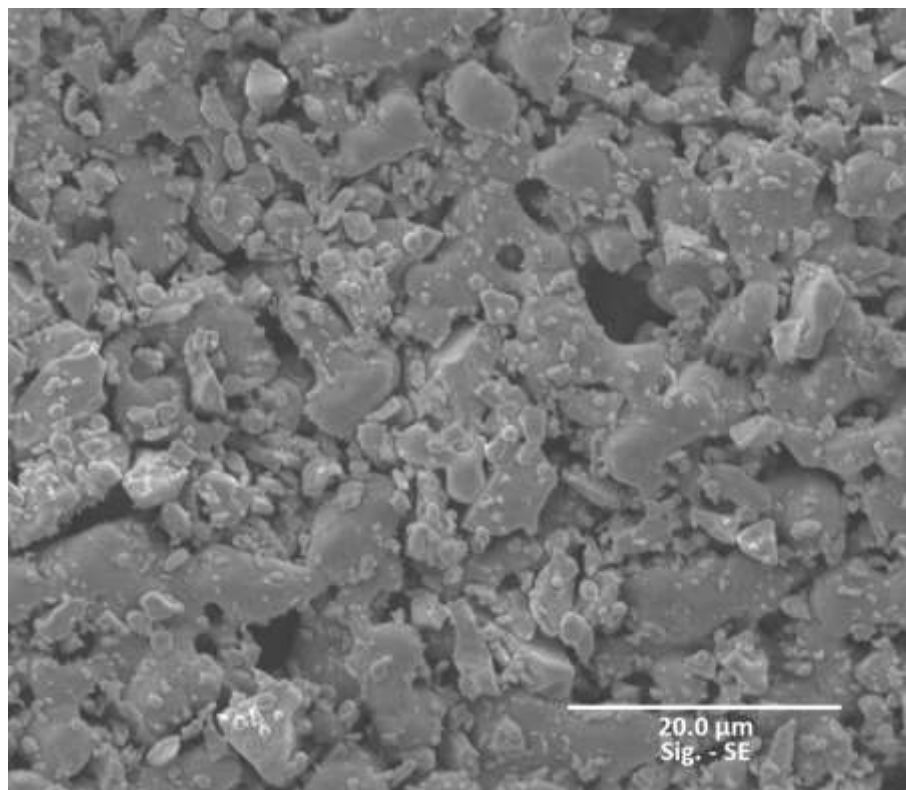


Figure 10. Secondary electron image of the fuel cell anode that had no spinel additions on the surface.

2. Fuel Cell With 0.015g of Spinel Added

The addition of 0.015g of spinel, applied via an isopropanol suspension, was an insufficient amount to completely cover the surface of the anode with spinel which can be seen in Figure 11 and Figure 12 with the darkest particles being the lower density spinel on the surface of the higher density Ni-YSZ cermet. In the images, nickel-copper alloy

nanoparticles have reduced out of the bulk spinel particles. The nanoparticles provide catalytically active sites for the reforming of CH_4 and CO_2 into H_2 and CO .

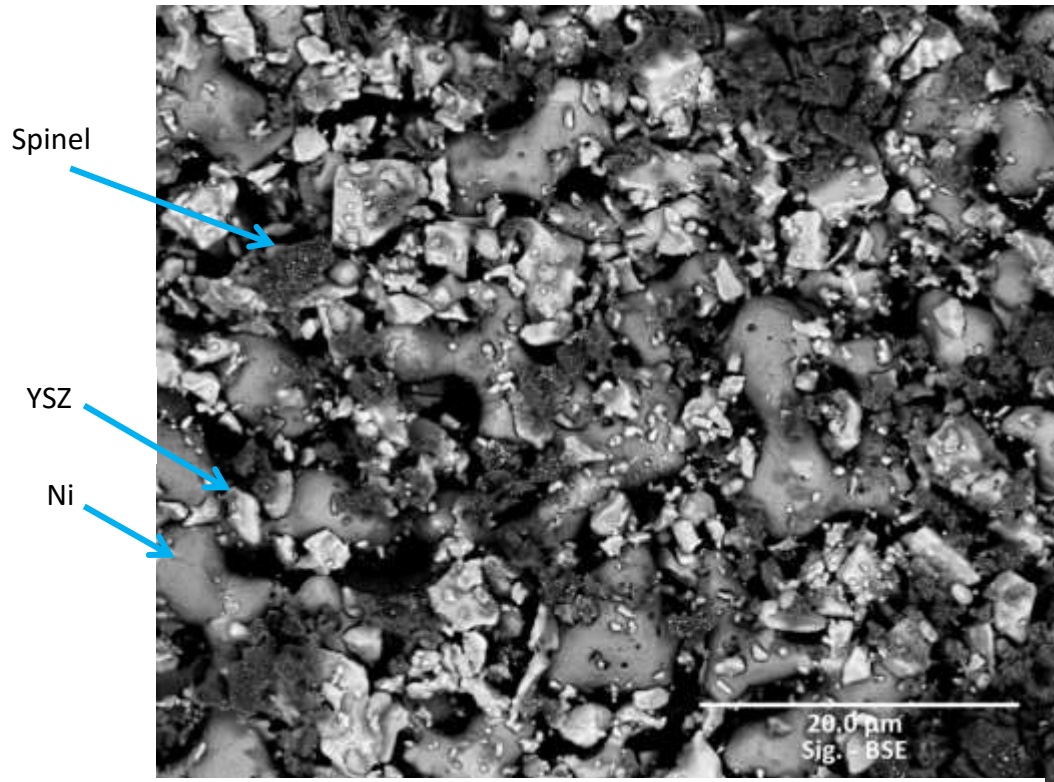


Figure 11. BSE image of 0.015g of spinel (darkest particles) added onto a Ni-YSZ anode.

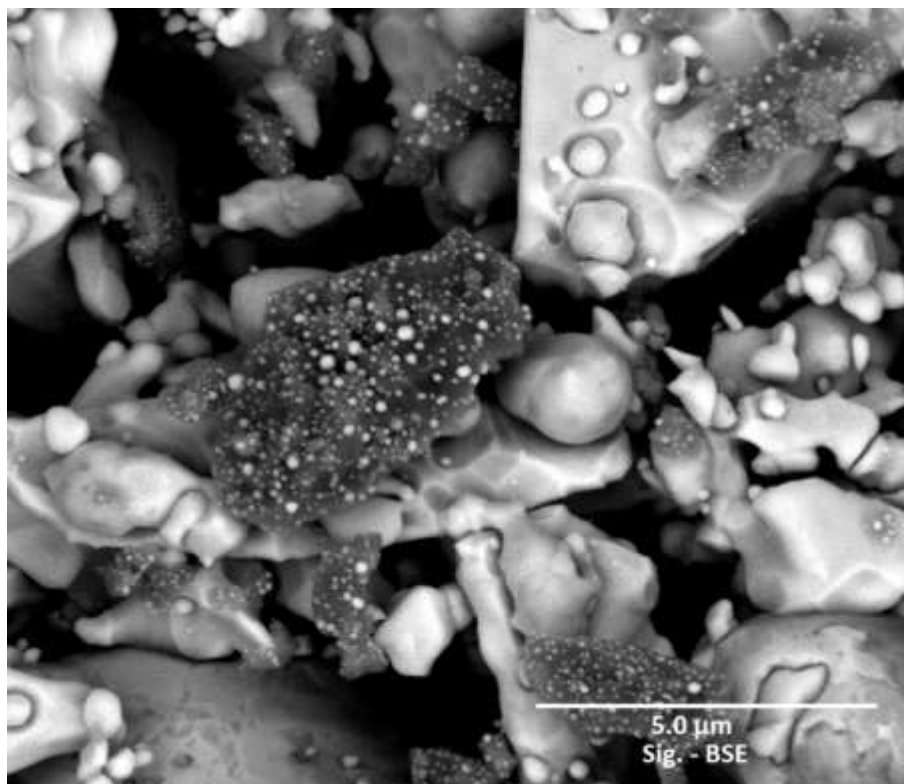
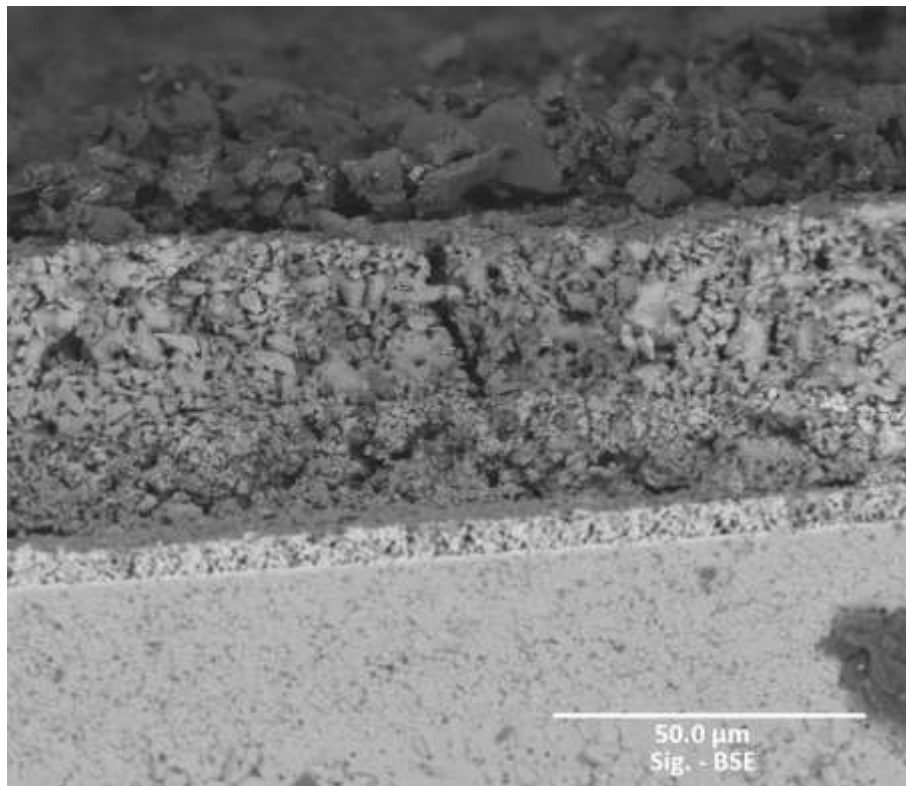
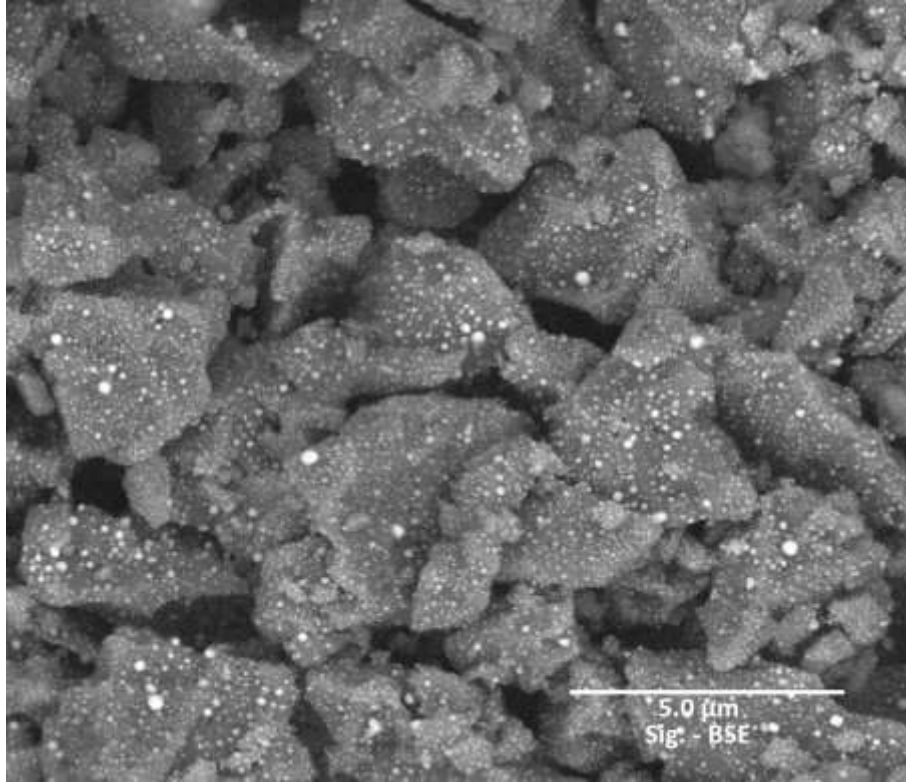


Figure 12. Backscattered electron image of spinel (dark particles), with nanoparticles on surface (bright spots), deposited on the Ni-YSZ anode.

3. Fuel Cell With 0.05g of Spinel Added

When 0.05g of spinel was applied via a sedimentation method, it was enough to cover the surface of the anode. After 96 hours on stream in the 1:1 CH₄:CO₂ gas mixture, the spinel layer does not show any fibrous carbon on the surface of the anode. (Figure 13 and Figure 14) Similar to Figure 12, there are nickel-copper alloy nanoparticles that have reduced out of the spinel onto the surface of the spinel. From Figure 14, it is possible to see that the platinum current collector will contact the more insulating spinel and less of the Ni-YSZ. Furthermore, since the more conductive Ni-Cu nanoparticles do not form a continuous network for the conduction of electrons, they will only have an effect on the reforming process. More images of the fuel cell after endurance testing can be found in Appendix D, which show the spinel on the surface of the anode for both 0.015 g and 0.05g additions.



Spinel
layer

Figure 14. Backscattered electron image of a fuel cell with full spinel coverage after endurance testing.

E. Raman Spectroscopy

Ex-situ Raman spectroscopy was completed on the endurance tested electrochemical performance fuel cells to determine if carbon deposition was present on the anode, and if so, in what form. The Raman spectra for the samples with no spinel, 0.015 g of added spinel, and 0.05 g of spinel additions can be seen in Figure 15. The fuel cell that had no spinel additions had four primary peaks at 1346, 1583, 2455, and 2720 cm^{-1} . These peaks are the fundamental peaks for graphitic carbon.⁶¹ The peak at 1346 cm^{-1} is the D band. The band at 1583 cm^{-1} is the G band, and the last two peaks are the 2D bands. The primary routes to carbon deposition on the anode are carbon monoxide disproportionation and methane cracking.⁶²

The Raman spectra for the two samples that had spinel added to the fuel cells do not show any carbon deposition on the surface of the anodes. (Figure 15) As the spinel is reforming the CH_4 into CO and H_2 , the methane concentration is decreasing. The decrease in methane concentration will also decrease the amount of methane cracking that occurs across the anode, limiting the amount of carbon deposition.

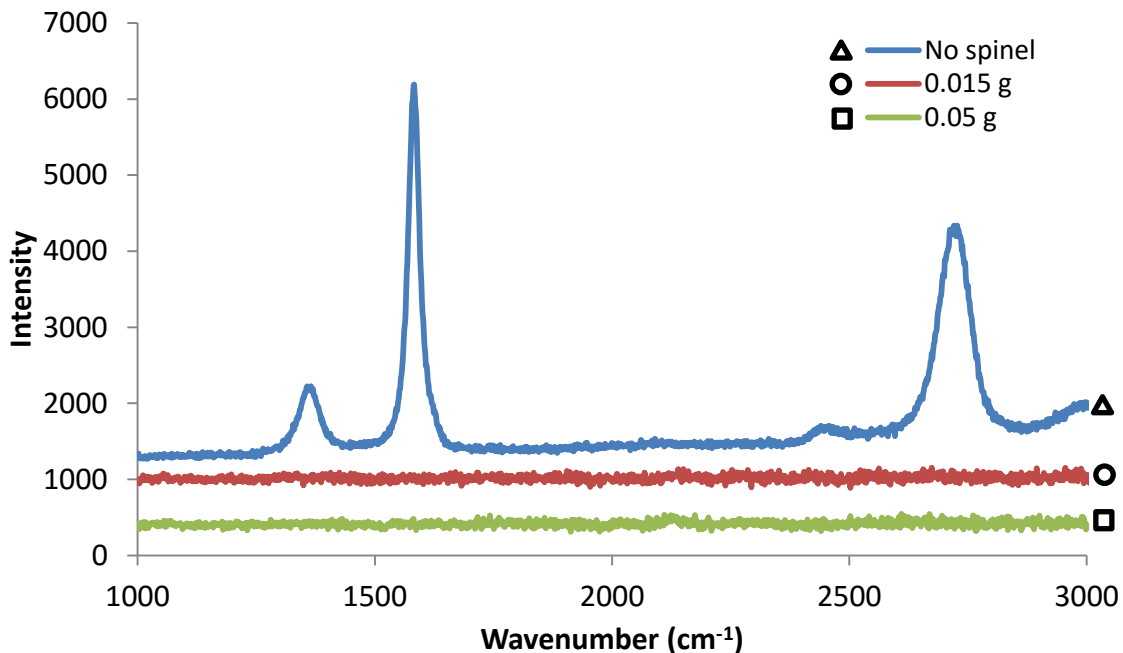


Figure 15. Ex-situ Raman spectra for endurance testing fuel cell samples.

DISCUSSION

A. Phase Compatibility

The composition of the spinel is particularly important to the reforming activity, especially the relative ratio of nickel to copper on the A-site. Copper is added to the spinel because it is well known that copper does not catalyze C-C bonds like nickel does.²³ Thus, when the spinel is reduced, Ni-Cu alloy nanoparticles reduce out of the spinel matrix.⁵⁷ The nanoparticles have the high catalytic activity of nickel while being less susceptible to carbon deposition thanks to the copper. A possible failure mechanism for the spinel catalysts on Ni-YSZ anodes is Ni enhancement and consequently Cu dilution. Therefore, when the spinel reacts with the nickel in the system there will be a change in the spinel stoichiometry to a higher nickel ratio on the A-site. This increase in nickel in the spinel will translate to an increase in nickel content in the nanoparticles and a decrease in the resistance to carbon deposition of the nanoparticles. However, with decreasing temperature, there is a decrease in the peak shift, indicating less reaction at lower temperatures, and at operation temperatures (below 1000°C) the reaction should not occur at all. (Figure 4 and Figure 5)

The XRD patterns also show YSZ peak shifts after reaction of the mixed powders. Rietveld refinement correlated the peak shift to a decrease in the YSZ lattice parameter of 0.02 +/- 0.00016 Angstroms which could be caused by Al substitutions in the lattice. Ji et al.⁶³ reported that 5 weight percent Al can be doped into the YSZ structure. Furthermore, Gao et al.⁶⁴ reported that when dopants with smaller atomic radii are added into the YSZ structure, there is an associated decrease in lattice parameters. However, both authors required temperatures above 1200°C to change the YSZ composition. Therefore, the reaction between the spinel and YSZ would only occur during fuel cell fabrication, and not during operation.

From a kinetic standpoint there are two limiting factors for either reaction to occur in an actual fuel cell system: surface area contact between the anode and spinel, and the available Al. In the current system, there is a large amount of surface area contact

between each of the fuel cell components, but in an actual fuel cell the only contact will be right at the interface between the reforming layer and the anode. With a decrease in surface area, the reaction rate will slow down. Furthermore, both reactions are utilizing Al, and since the Al is already in the stable spinel phase, and there was no huge degradation of the spinel in the study, it is unlikely that the reactions will occur to an extent during fabrication that is detrimental to the system.

B. Coefficient of Thermal Expansion (CTE)

The coefficients of thermal expansion of the fuel cell components must match well enough to prevent thermal stress from causing failure upon startup and shutdown procedures.¹ As previously stated, the most commonly used materials in SOFCs are a LSM cathode, a YSZ electrolyte, and a Ni-YSZ cermet anode which has the highest CTE.⁶⁵ Mori et al⁶⁶ reported that the CTE of the Ni-YSZ cermet depended on the Ni:YSZ ratio, with a 1 Ni: 1 YSZ anode having a CTE of about $14.5 \times 10^{-6} \text{ K}^{-1}$ from 25°C to 1000°C. This means that compared to a 1 Ni: 1 YSZ cermet anode, the oxide spinel (with a CTE of $10 \times 10^{-6} \text{ K}^{-1}$) will expand 31% less during heating and cooling of the SOFC stacks. As a reference point, the 8 YSZ electrolyte has a CTE that is about 28% less than that of 1 Ni: 1 YSZ cermet anode.¹⁷ The effects that the large difference in thermal expansion would have on the fuel cell in an SOFC stack depend on the thickness of the reforming layer compared to the thickness of the anode because the induced stress will vary, but the large difference in thermal expansion will likely cause cracking during startup and shutdown procedures for high temperature operations. In intermediate temperature SOFCs, which operate at temperatures ranging from 550 to 750°C, the thermal expansion mismatch would not have as much of an effect. In a similar situation, Kwak et al.⁶⁰ applied an internal reforming layer of NiO-MAI₂O₄ (M= Cu, Co, Ni) and added up to 50 weight % NiO to increase the CTE of the reforming layer to better match that of Ni-YSZ. However, adding excess nickel to the catalyst layer does not solve the problem, because the catalytic layer would then be prone to carburization and all the other shortcomings of nickel. Therefore, the best

option would be to utilize the spinel reforming layer in an intermediate temperature SOFC.

C. Electrochemical Performance

1. Operation Under 4% H₂

While operating under a 4% H₂ fuel gas there was no significant change in the power density output of the fuel cells with 0.015g of spinel and fuel cells without spinel additions. The similar power densities were caused by two things: the spinel not completely covering the anode, leaving exposed Ni-YSZ anode to contact the platinum interconnect, and H₂ not needing to be reformed by the spinel. Since H₂ is already the optimal fuel for a Ni-YSZ anode, and does not require any reforming, the spinel is not participating in any of the electrochemical reactions while operating with H₂. Therefore, the addition of spinel would not increase the performance of the fuel cell from an electrochemical reaction perspective. However, the spinel could reduce the conduction of electrons from the anode to the platinum current collector. Compared to Ni, which has an electrical conductivity of $138 \times 10^4 \text{ S}\cdot\text{cm}^{-1}$ at 25°C¹⁷, the spinel has a significantly lower electrical conductivity. After the Ni-Cu nanoparticles have been reduced out of the bulk, the remnant spinel will be MgAl₂O₄.⁶⁷ Padmaraj et al.⁶⁸ reported that the electrical conductivity of MgAl₂O₄ spinel at 150°C is approximately $2.5 \times 10^{-16} \text{ S}\cdot\text{cm}^{-1}$. Therefore, the more spinel the current collector is contacting, the larger the effective resistivity of the anode, translating to a decrease in power density. However, as previously mentioned, the addition of 0.015g of spinel was not enough to completely cover the anode. The spinel only covered about 15% of the anode surface. The coverage of 15% of the anode would cause a higher contact resistance between the anode and the interconnect, but since the current collector could contact 85% of the Ni-YSZ, the effect of the contact resistance was negligible. Therefore, with no change in the electrochemical reaction rate of the cell and little change in the electrical conductivity, the peak power densities of the fuel cell did not change when 0.015 g of spinel was added.

2. Operation Under Methane-Carbon Dioxide Gas Mixtures

It is well known that variables such as temperature, oxygen:carbon ratio (O:C), hydrogen:carbon ratio (H:C), and pressure influence the likelihood of carbon deposition on the anode.^{69,70} As previously stated, carbon deposition is more likely to occur at high temperatures with low O:C and O:H ratios, but can be limited with the addition of steam.¹⁷ In the current work, two dry methane-carbon dioxide gas mixtures were used in the electrochemical testing: a coking gas mixture containing 47.5% CH₄ - 47.5% CO₂ - 5% N₂ (O:C=1 and H:C=2), and a non-coking mixture consisting of 32% CH₄ - 63% CO₂ - 5% N₂ (O:C=4:3 and H:C=4:3). Therefore, with such low O:C and H:C ratios in the fuel gases, operating without any steam additions, and at temperatures of 750°C and 850°C carbon deposition was favored during the electrochemical testing of the fuel cells. In commercial use, steam would be added to reduce the effects of coking, but the large amount of steam that is necessary for steam reforming increases operational cost, decreases the electrical efficiency because of fuel dilution, and makes the anode atmosphere significantly more corrosive. In addition, the endothermic nature of steam reforming can cause steep thermal gradients to form. These thermal gradients, if large enough, can cause mechanical failure of the fuel cell to occur.¹⁷

As stated previously, the electrical conductivity of spinel type materials is not nearly as high as the electrical conductivity of Ni or Ni-YSZ cermets. To improve the conductivity of the reforming layer, other authors such as Wang et al.⁴² and Srisuwan et al.⁵⁶ have made Ni-spinel composite materials using as much as 60% nickel. Although the addition of nickel did improve the conductivity of the anode, that option was not practical for this study. In our composite anodes, the purpose of adding the spinel to the anode is because nickel-copper alloy nanoparticles can be reduced out of the spinel. The nanoparticles are catalytically active sites for fuel reforming, with a large specific surface area, and can be regenerated through redox cycling if deactivated through carbon deposition or sulfur poisoning.⁵⁷ As discussed previously, the Ni:Cu ratio in the nanoparticles is important to the coking resistance and additional Ni might cause dilution of the Cu to an extent that reduces the coking resistance.

After the spinel is reduced, well-dispersed Ni-Cu alloy nanoparticles with high specific surface area form on the surface of the spinel.⁵⁶ These nanoparticles increase reforming of the incoming CH₄ and CO₂ fuel gas into H₂ and CO according to equation 3. The available H₂ and CO will then diffuse to the anode active layer where they will be electrochemically oxidized at the triple phase boundary to produce H₂O, CO₂, and 2e⁻. It is known that nickel-based cermet anodes have a higher electrochemical activity for H₂ and CO than for CH₄⁴⁵, so the cell with spinel additions has a higher power output than the cell without. When the fuel cells were operated under the non-coking fuel gas of 32% CH₄ – 63% CO₂ -5% N₂, the addition of 0.015 g of spinel increased the power densities from 74 mW·cm⁻² at 850°C and 40 mW·cm⁻² at 750°C to 98 mW·cm⁻² and 56 mW·cm⁻², respectively, which is approximately 30% increase in peak power density at both temperatures. As previously discussed, the fuel cell with 0.015 g of spinel maintains a low contact resistance between the anode and the interconnect, but this time the fuel cell also benefited from the spinel increasing the reforming rate of methane.

Misture et al.⁵⁷ reported that in a 12 hour catalyst test at 850°C, with a gas hourly space velocity (GHSV) of 60,000, 2 mL, approximately 0.84 g, of Ni_{0.375}Cu_{0.375}Mg_{0.25}Al₂O₄ was able to reform an average of 27% of the incoming methane. Due to the inherent differences in catalyst testing and electrochemical testing systems for SOFCs, it is difficult to accurately determine how much of the incoming methane is reformed by the spinel. However, it is clear that the small amount of spinel that was added to the fuel cell was insufficient to reform all of the incoming fuel gas. Therefore, carburization reactions such as methane cracking and carbon monoxide disproportionation still occurred across the Ni-YSZ anode. The addition of 0.05 g of spinel did not improve the power density of the fuel cell while operating under the dry methane – carbon dioxide fuel gas. As seen in Figure 13, the spinel covers more of the anode, which means that the platinum current collector was contacting less of the Ni-YSZ, and more of the insulating spinel phase during electrochemical testing. The contact with the spinel phase increases the resistance of the anode, translating to a low power density. The higher resistance was demonstrated when the conductivity was measured for Ni-spinel composites and compared to that of Ni-YSZ.⁷¹

It was noted that the Ni-spinel composites had a higher resistivity than Ni-YSZ which caused a decrease in the electrochemical performance of the fuel cells. Compared to 0.015 g of spinel additions, 0.05 g of spinel should increase the amount of CH₄ and CO₂ reformed by a factor of 3. However, this increase is still insufficient to reform all of the incoming methane. Thus carbon deposition could still occur on the Ni-YSZ anode.

D. Scanning Electron Microscopy and Raman Spectra

Carbon deposition covers the active sites of the anode, resulting in the loss of cell performance. Carbon can form various structures including adsorbed, polymeric, carbide, vermicular filaments, and graphitic, with graphitic carbon being the most common on anodes.⁷² The types of carbon variously degrade reactivity and increase the extent of catalyst deactivation.^{17,19} However, the amount and stability of carbon deposits formed on Ni-YSZ can be affected by current density, exposure time, water content in the fuel gas, and anode thickness.⁶² In all of the SEM images, no carbon fibers were observed.

The Raman spectrum for the fuel cell that does not have any spinel additions shows that the fingerprint bands of graphitic carbon are present on the anode, whereas the fuel cells with spinel additions do not have any graphitic carbon bands in the spectra. The band at 1350 cm⁻¹ is the D band for graphite. The band at 1585 cm⁻¹ is the graphite G band. The G band is the fundamental carbon peak which arises from the honeycomb structure of carbon. At 2700 cm⁻¹ is the 2D band for carbon. The 2D band arises from the resonant interaction between the incident light and the electronic structure of carbon.⁶¹

Carbon deposition on the anode occurs through two primary routes: methane cracking (equation 3) and carbon monoxide disproportionation (equation 4). Nikoo et al.³⁸ reported that at 850°C, with a CO₂:CH₄ ratio equal to 1, carbon deposition is favorable for a Ni-YSZ cermet anode. It is known that nickel catalyzes the methane cracking reaction.⁷³ However, the carbon can then be oxidized with CO₂, via the reverse CO disproportionation reaction.⁷⁴ The decrease in carbon on the fuel cell anode was attributed to the spinel increasing the reforming rate of the fuel gases prior to contact with the anode.

SUMMARY AND CONCLUSIONS

$\text{Ni}_{0.375}\text{Cu}_{0.375}\text{Mg}_{0.25}\text{Al}_2\text{O}_4$ was investigated for its use as a reforming catalyst for solid oxide fuel cell anodes. At temperatures of 1300°C- 1500°C, the spinel was found to react with available nickel to form additional spinel; however, the reaction would not be extensive enough to cause detrimental effects to the fuel cell's performance.

The coefficient of thermal expansion was calculated from Rietveld refinements of the HTXRD patterns to be $10 \times 10^{-6} \text{ K}^{-1}$, which is lower than any other fuel cell material currently used in state-of-the-art fuel cells. Therefore, the addition of a spinel reforming layer will cause stress on the fuel cell during startup and shutdown procedures, which could lead to mechanical failure of the SOFC during high temperature operation. The CTE difference will not have as significant an effect for IT-SOFC applications.

The electrochemical performance of the fuel cells was dependent on two factors: the amount of spinel added and the ability of the anode to efficiently conduct charge. The addition of 0.015 g of spinel had no effect on the peak power density when operating under a 4% H_2 atmosphere due to H_2 not needing to be reformed and the platinum interconnect being able to contact the Ni-YSZ anode. In addition, 0.015 g of spinel increased the power density by as much as 30% while operating under non-coking methane fuel gas mixture, and 27% increase under a coking methane fuel gas. The increase in power density was attributed to the platinum interconnect contacting the more conductive nickel, while the spinel increased the reforming rate of methane to produce more H_2 and CO. It was observed that when the interconnect was contacting only spinel, as it did in the samples with 0.05g spinel addition, the peak power density dropped approximately 8% while operating under the coking methane fuel gas mixture. The drop in power density was attributed to an increase in ohmic resistance at the anode.

Post electrochemical performance characterization of the fuel cells using SEM showed no carbon fibers on the anode. However, *ex-situ* Raman shift spectra of the endurance testing samples indicate graphitic carbon is on the fuel cell with no spinel additions. In

contrast, no graphitic carbon bands were present in the spectra for samples with spinel additions.

Unless the CTE mismatch of $\text{Ni}_{0.375}\text{Cu}_{0.375}\text{Mg}_{0.25}\text{Al}_2\text{O}_4$ and the SOFC anode can be resolved, $\text{Ni}_{0.375}\text{Cu}_{0.375}\text{Mg}_{0.25}\text{Al}_2\text{O}_4$ is not suitable as a reforming catalyst for high temperature SOFCs. However, in an intermediate temperature SOFC, where CTE mismatch does not have such a large effect, $\text{Ni}_{0.375}\text{Cu}_{0.375}\text{Mg}_{0.25}\text{Al}_2\text{O}_4$ could be used. Furthermore, additional research is needed to optimize the processing of the reforming layer and application to the anode.

FUTURE WORK

To evaluate the full potential of the catalyst reforming layer, the processing and application of the spinel to the anode should be optimized. Since the low electrical conductivity of the spinel diminishes the power density, the fuel cell should be fabricated in such a way that the current collector is beneath the reforming layer. Furthermore, long term stability of the spinel and anode components should be evaluated at the intermediate temperature SOFC range.

REFERENCES

1. S. C. Singhal, "Advances in Solid Oxide Fuel Cell Technology," *Solid State Ionics*, **135** [1–4] 305-13 (2000).
2. A. B. Stambouli and E. Traversa, "Solid Oxide Fuel Cells (SOFCs): A Review of an Environmentally Clean and Efficient Source of Energy," *Renewable Sustainable Energy Rev.*, **6** [5] 433-55 (2002).
3. O. Yamamoto, "Solid Oxide Fuel Cells: Fundamental Aspects and Prospects," *Electrochim. Acta*, **45** [15–16] 2423-35 (2000).
4. H.-H. Möbius, "History"; pp. 23-44 in *High Temperature Solid Oxide Fuel Cells: Fundamentals, Design and Application*. Edited by K. K. S. C. Singhal. Elsevier, New York, Oxford, UK, 2, 2003.
5. K. K. S. C. Singhal, "Introduction to SOFCs"; pp. 1-19 in *High Temperature Solid Oxide Fuel Cells: Fundamentals, Design and Applications*. Edited by K. K. S. C. Singhal. Elsevier, New York, Oxford, UK, 1, 2003.
6. K. M. McDevitt, "Improving Solid Oxide Fuel Cell Cathode Stability with Chemical Substitutions"; Master of Science in Ceramic Engineering Thesis. Alfred University, 2013.
7. "Cool Fuel cells" NASA Science. Accessed on: July 2016. Available at http://science.nasa.gov/science-news/science-at-nasa/2003/18mar_fuelcell/ >
8. T. H. H. Yokokawa, "Cathodes"; in *High Temperature Solid Oxide Fuel Cells*. Edited by K. K. S. C. Singhal. Elsevier, New York, Oxford, UK, 5, 2003.
9. N. M. S. T. Ishihara, O. Yamamoto, "Electrolytes"; in *High Temperature Solid Oxide Fuel Cells*. Edited by K. K. S. C. Singhal. Elsevier, New York, Oxford, UK, 4, 2003.
10. E. G. T. Services, "Fuel Cell Handbook (Seventh Edition)," Department of Energy Morgantown, West Virginia, 2004.
11. A. McEvoy, "Anodes"; in *High temperature Solid Oxide Fuel Cells*. Edited by K. K. S. C. Singhal. Elsevier, New York, Oxford, UK, 6, 2003.
12. J. M. Ralph, A. C. Schoeler, and M. Krumpelt, "Materials for Lower Temperature Solid Oxide Fuel Cells," *J. Mater. Sci.*, **36** [5] 1161-72 (2001).

13. P. Holtappels, L. G. J. D. Haart, U. Stimming, I. C. Vinke, and M. Mogensen, "Reaction of CO/CO₂ gas mixtures on Ni-YSZ cermet electrodes," *J. Appl. Electrochem.*, **29** [5] 561-8 (1999).
14. O. Costa-Nunes, R. J. Gorte, and J. M. Vohs, "Comparison of the Performance of Cu-CeO₂-YSZ and Ni-YSZ Composite SOFC Anodes with H₂, CO, and Syngas," *J. Power Sources*, **141** [2] 241-9 (2005).
15. A. Weber, B. Sauer, A. C. Müller, D. Herbstritt, and E. Ivers-Tiffée, "Oxidation of H₂, CO and Methane in SOFCs with Ni/YSZ-Cermet Anodes," *Solid State Ionics*, **152-153** 543-50 (2002).
16. K. M. Ong, W. Y. Lee, J. Hanna, and A. F. Ghoniem, "Isolating the Impact of CO Concentration in Syngas Mixtures on SOFC Performance Via Internal Reforming and Direct Oxidation," *Int. J. Hydrogen Energy*, **41** [21] 9035-47 (2016).
17. B. Shri Prakash, S. Senthil Kumar, and S. T. Aruna, "Properties and Development of Ni/YSZ as an Anode Material in Solid Oxide Fuel Cell: A Review," *Renewable Sustainable Energy Rev.*, **36** 149-79 (2014).
18. Y. Lin, Z. Zhan, J. Liu, and S. A. Barnett, "Direct Operation of Solid Oxide Fuel Cells with Methane Fuel," *Solid State Ionics*, **176** [23-24] 1827-35 (2005).
19. V. N. Nguyen, R. Deja, R. Peters, and L. Blum, "Methane/Steam Global Reforming Kinetics Over the Ni/YSZ of Planar Pre-Reformers for SOFC Systems," *Chem. Eng. J.*, **292** 113-22 (2016).
20. D. Simwonis, F. Tietz, and D. Stöver, "Nickel Coarsening in Annealed Ni/8YSZ Anode Substrates for Solid Oxide Fuel Cells," *Solid State Ionics*, **132** [3-4] 241-51 (2000).
21. M. Cassidy, G. Lindsay, and K. Kendall, "The Reduction of Nickel-Zirconia Cermet Anodes and the Effects on Supported Thin Electrolytes," *J. Power Sources*, **61** [1] 189-92 (1996).
22. S. Park, J. M. Vohs, and R. J. Gorte, "Direct Oxidation of Hydrocarbons in a Solid-Oxide Fuel Cell," *Nature*, **404** [6775] 265-7 (2000).
23. K. Park, S. Lee, G. Bae, and J. Bae, "Performance Analysis of Cu, Sn and Rh Impregnated NiO/CGO91 Anode for Butane Internal Reforming SOFC at Intermediate Temperature," *Renewable Energy*, **83** 483-90 (2015).
24. S. Tao and J. T. S. Irvine, "A Redox-Stable Efficient Anode for Solid-Oxide Fuel Cells," *Nat. Mater.*, **2** [5] 320-3 (2003).

25. C. Zhang, Y. Zheng, Y. Lin, R. Ran, Z. Shao, and D. Farrusseng, "A Comparative Study of $\text{La}_{0.8}\text{Sr}_{0.2}\text{MnO}_3$ and $\text{La}_{0.8}\text{Sr}_{0.2}\text{Sc}_{0.1}\text{Mn}_{0.9}\text{O}_3$ as Cathode Materials of Single-Chamber SOFCs Operating on a Methane–Air Mixture," *J. Power Sources*, **191** [2] 225-32 (2009).
26. J. Wan, J. H. Zhu, and J. B. Goodenough, " $\text{La}_{0.75}\text{Sr}_{0.25}\text{Cr}_{0.5}\text{Mn}_{0.5}\text{O}_{3-\delta}$ + Cu Composite Anode Running on H_2 and CH_4 Fuels," *Solid State Ionics*, **177** [13–14] 1211-7 (2006).
27. A. Ovalle, J. C. Ruiz-Morales, J. Canales-Vázquez, D. Marrero-López, and J. T. S. Irvine, "Mn-Substituted Titanates as Efficient Anodes for Direct Methane SOFCs," *Solid State Ionics*, **177** [19–25] 1997-2003 (2006).
28. Y.-H. Huang, R. I. Dass, Z.-L. Xing, and J. B. Goodenough, "Double Perovskites as Anode Materials for Solid-Oxide Fuel Cells," *Science*, **312** [5771] 254-7 (2006).
29. J. B. Goodenough and Y.-H. Huang, "Alternative Anode Materials for Solid Oxide Fuel Cells," *J. Power Sources*, **173** [1] 1-10 (2007).
30. B. D. Madsen, W. Kobsiriphat, Y. Wang, L. D. Marks, and S. A. Barnett, "Nucleation of Nanometer-Scale Electrocatalyst Particles in Solid Oxide Fuel Cell Anodes," *J. Power Sources*, **166** [1] 64-7 (2007).
31. S. Zha, Z. Cheng, and M. Liu, "A Sulfur-Tolerant Anode Material for SOFCs," *Electrochem. Solid-State Lett.*, **8** [8] A406-A8 (2005).
32. Z. Du, H. Zhao, X. Zhou, Z. Xie, and C. Zhang, "Electrical Conductivity and Cell Performance of $\text{La}_{0.3}\text{Sr}_{0.7}\text{Ti}_{1-x}\text{Cr}_x\text{O}_{3-\delta}$ Perovskite Oxides Used as Anode and Interconnect Material for SOFCs," *Int. J. Hydrogen Energy*, **38** [2] 1068-73 (2013).
33. S.-H. Cui, J.-H. Li, A. Jayakumar, J.-L. Luo, K. T. Chuang, J. M. Hill, and L.-J. Qiao, "Effects of H_2S and H_2O on Carbon Deposition Over $\text{La}_{0.4}\text{Sr}_{0.5}\text{Ba}_{0.1}\text{TiO}_3/\text{YSZ}$ Perovskite Anodes in Methane Fueled SOFCs," *J. Power Sources*, **250** 134-42 (2014).
34. Y.-F. Sun, J.-H. Li, K. T. Chuang, and J.-L. Luo, "Electrochemical Performance and Carbon Deposition Resistance of Ce-Doped $\text{La}_{0.7}\text{Sr}_{0.3}\text{Fe}_{0.5}\text{Cr}_{0.5}\text{O}_{3-\delta}$ Anode Materials for Solid Oxide Fuel Cells Fed With Syngas," *J. Power Sources*, **274** 483-7 (2015).
35. X. Wu, X. Zhou, Y. Tian, X. Kong, J. Zhang, W. Zuo, and X. Ye, "Stability and Electrochemical Performance of Lanthanum Ferrite-Based Composite SOFC Anodes in Hydrogen and Carbon Monoxide," *Electrochim. Acta*, **208** 164-73 (2016).

36. E. P. Murray, T. Tsai, and S. A. Barnett, "A Direct-Methane Fuel Cell With a Ceria-Based Anode," *Nature*, **400** [6745] 649-51 (1999).
37. Z. Zhan and S. A. Barnett, "An Octane-Fueled Solid Oxide Fuel Cell," *Science*, **308** [5723] 844-7 (2005).
38. N. A. S. A. M. Khoshtinat Nikoo, "Thermodynamic Analysis of Carbon Dioxide Reforming of Methane in View of Solid Carbon Formation," *Fuel Process. Technol.*, 678-91 (2011).
39. A. Wolfbeisser, O. Sophiphun, J. Bernardi, J. Wittayakun, K. Föttinger, and G. Rupprechter, "Methane Dry Reforming Over Ceria-Zirconia Supported Ni Catalysts," *Catal. Today*, (2016).
40. N. Salhi, A. Boulahouache, C. Petit, A. Kiennemann, and C. Rabia, "Steam Reforming of Methane to Syngas Over NiAl₂O₄ Spinel Catalysts," *Int. J. Hydrogen Energy*, **36** [17] 11433-9 (2011).
41. A. F. Ibarreta and C.-J. Sung, "Optimization of Jet-A Fuel Reforming for Aerospace Applications," *Int. J. Hydrogen Energy*, **31** [8] 1066-78 (2006).
42. M. Usman, W. M. A. Wan Daud, and H. F. Abbas, "Dry Reforming of Methane: Influence of Process Parameters—A Review," *Renewable Sustainable Energy Rev.*, **45** 710-44 (2015).
43. C. Guerra, A. Lanzini, P. Leone, M. Santarelli, and N. P. Brandon, "Optimization of Dry Reforming of Methane Over Ni/YSZ Anodes for Solid Oxide Fuel Cells," *J. Power Sources*, **245** 154-63 (2014).
44. C. Jin, C. Yang, F. Zhao, A. Coffin, and F. Chen, "Direct-Methane Solid Oxide Fuel Cells with Cu_{1.3}Mn_{1.7}O₄ Spinel Internal Reforming Layer," *Electrochem. Commun.*, **12** [10] 1450-2 (2010).
45. C. Jin, C. Yang, H. Zheng, and F. Chen, "Intermediate Temperature Solid Oxide Fuel Cells with Cu_{1.3}Mn_{1.7}O₄ Internal Reforming Layer," *J. Power Sources*, **201** 66-71 (2012).
46. W. Wang, W. Zhou, R. Ran, R. Cai, and Z. Shao, "Methane-Fueled SOFC with Traditional Nickel-Based Anode by Applying Ni/Al₂O₃ as a Dual-Functional Layer," *Electrochem. Commun.*, **11** [1] 194-7 (2009).
47. X. Song, X. Dong, M. Li, and H. Wang, "Effects of Adding Alumina to the Nickel-Zirconia Anode Materials for Solid Oxide Fuel Cells and a Two-Step Sintering Method for Half-Cells," *J. Power Sources*, **308** 58-64 (2016).

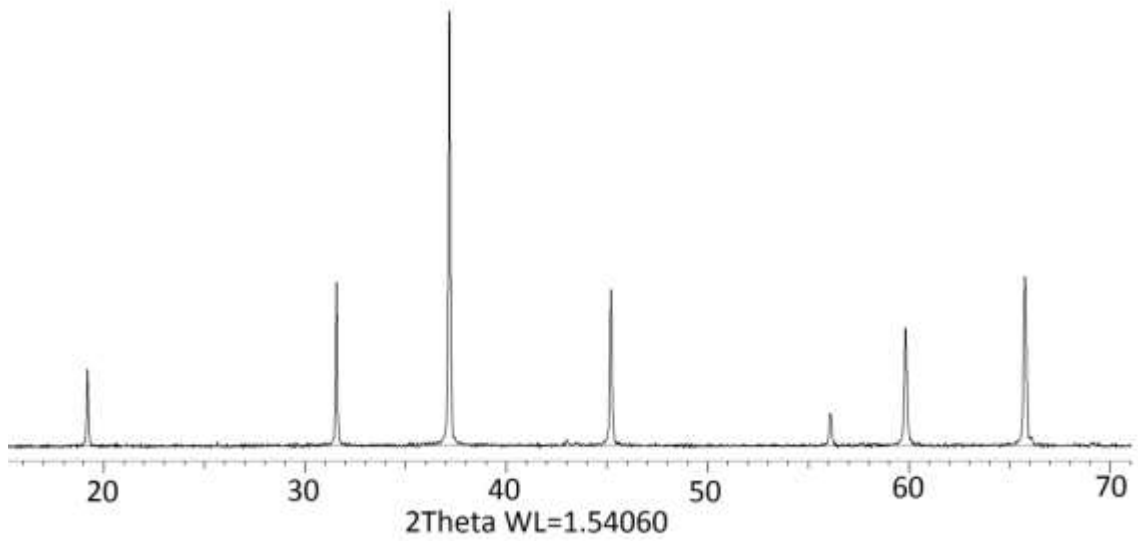
48. D. N. Jaeha Myung, Mark Tham and John T. S. Irvine, "In Situ Tailored Nickel Nano-Catalyst Layer for Internal Reforming Hydrocarbon Fueled SOFCs," *ECS Trans.*, **68** 1121-8 (2015).
49. F. Wang, W. Wang, R. Ran, M. O. Tade, and Z. Shao, "Aluminum Oxide as a Dual-Functional Modifier of Ni-Based Anodes of Solid Oxide Fuel Cells for Operation on Simulated Biogas," *J. Power Sources*, **268** 787-93 (2014).
50. W. Winkler, "Thermodynamics"; pp. 53-81 in *High Temperature Solid oxide fuel cells*. Edited by K. K. S. C. Singhal. Elsevier, New York, Oxford, UK, 3, 2003.
51. A. V. V. Ellen Ivers- Tiffée, "Electrode Polarisation"; pp. 229-60 in *High Temperature Solid Oxide Fuel Cells*. Edited by S. C. Singhal. Elsevier, 2003.
52. E. L. Foletto, R. W. Alves, and S. L. Jahn, "Preparation of Ni/Pt Catalysts Supported on Spinel (MgAl₂O₄) for Methane Reforming," *J. Power Sources*, **161** [1] 531-4 (2006).
53. D. Li, T. Shishido, Y. Oumi, T. Sano, and K. Takehira, "Self-Activation and Self-Regenerative Activity of Trace Rh-Doped Ni/Mg(Al)O Catalysts in Steam Reforming of Methane," *Appl. Catal., A*, **332** [1] 98-109 (2007).
54. S. Sá, H. Silva, L. Brandão, J. M. Sousa, and A. Mendes, "Catalysts for Methanol Steam Reforming—A review," *Appl. Catal., B*, **99** [1–2] 43-57 (2010).
55. J. Kehres, J. W. Andreasen, J. B. Fløystad, H. Liu, A. Molenbroek, J. G. Jakobsen, I. Chorkendorff, J. H. Nielsen, K. Høydalsvik, D. W. Breiby, and T. Vegge, "Reduction of a Ni/Spinel Catalyst for Methane Reforming," *J. Phys. Chem. C*, **119** [3] 1424-32 (2015).
56. B. E. Hill and S. T. Misture, "Atomic Scale Mechanisms of the Reduction of Nickel-Magnesium Aluminate Spinel," *J. Am. Ceram. Soc.*, **96** [11] 3603-8 (2013).
57. S. M. Misture, KM; Glass, KC; Edwards, DD; Howe, JY; Rector, KD; He, H; Vogel, SC, "Sulfur-Resistant and Regenerable Ni/Co Spinel-Based Catalysts for Methane Dry Reforming," *Catal. Sci. Technol.*, **5** 4565-5474 (2015).
58. Y. Tanaka, R. Kikuchi, T. Takeguchi, and K. Eguchi, "Steam Reforming of Dimethyl Ether Over Composite Catalysts of γ -Al₂O₃ and Cu-Based Spinel," *Appl. Catal., B*, **57** [3] 211-22 (2005).
59. T. J. M.O. Naylor, J.E. Shelby, S.T. Misture, "Galliosilicate Glasses for Viscous Sealants in Solid Oxide Fuel Cell Stacks: Part I: Compositional Design," *Int. J. Hydrogen Energy*, **38** 16300-7 (2013).

60. B. H. Kwak, H. K. Youn, and J. S. Chung, "Ni and Metal Aluminate Mixtures for Solid Oxide Fuel Cell Anode Supports," *J. Power Sources*, **185** [2] 633-40 (2008).
61. V. D. R. C. Maher, G. J. Offer, M. Kishimoto, N. P. Brandon, L. F. Cohen, "Raman Spectroscopy of Solid Oxide Fuel Cells: Technique Overview and Application to Carbon Deposition Analysis," *Fuel Cells*, (2013).
62. Y. Jiao, L. Zhang, W. An, W. Zhou, Y. Sha, Z. Shao, J. Bai, and S.-D. Li, "Controlled Deposition and Utilization of Carbon on Ni-YSZ Anodes of SOFCs Operating on Dry Methane," *Energy*, **113** 432-43 (2016).
63. Y. Ji, J. Liu, Z. Lü, X. Zhao, T. He, and W. Su, "Study on the Properties of Al₂O₃-Doped (ZrO₂)_{0.92}(Y₂O₃)_{0.08} Electrolyte," *Solid State Ionics*, **126** [3-4] 277-83 (1999).
64. H. Gao, J. Liu, H. Chen, S. Li, T. He, Y. Ji, and J. Zhang, "The Effect of Fe Doping on the Properties of SOFC Electrolyte YSZ," *Solid State Ionics*, **179** [27-32] 1620-4 (2008).
65. W. H. K. V. Thangadurai, "Challenges and Prospects of Anodes for Solid Oxide Fuel Cells (SOFCs)," *Ionics*, **21** 301-18 (2015).
66. M. Mori, T. Yamamoto, H. Itoh, H. Inaba, and H. Tagawa, "Thermal Expansion of Nickel-Zirconia Anodes in Solid Oxide Fuel Cells during Fabrication and Operation," *J. Electrochem. Soc.*, **145** [4] 1374-81 (1998).
67. B. E. Hill, "Characterizing the Reduction of Ni_xMg_{1-x}Al₂O₄"; Doctor of Philosophy in Ceramics Thesis. Alfred University, 2012.
68. O. Padmaraj, M. Venkateswarlu, and N. Satyanarayana, "Structural, Electrical and Dielectric Properties of Spinel Type MgAl₂O₄ Nanocrystalline Ceramic Particles Synthesized by the Gel-Combustion Method," *Ceram. Int.*, **41** [2, Part B] 3178-85 (2015).
69. J. H. Edwards and A. M. Maitra, "Trends in Natural Gas Utilisation The Chemistry of Methane Reforming with Carbon Dioxide and its Current and Potential Applications," *Fuel Process. Technol.*, **42** [2] 269-89 (1995).
70. S. C. Tsang, J. B. Claridge, and M. L. H. Green, "Recent Advances in C1 Chemistry Recent Advances in the Conversion of Methane to Synthesis Gas," *Catal. Today*, **23** [1] 3-15 (1995).

71. L. Kou and J. R. Selman, "Electrical Conductivity and Chemical Diffusivity of NiAl₂O₄ Spinel Under Internal Reforming Fuel Cell Conditions," *J. Appl. Electrochem.*, **30** [12] 1433-7 (2000).
72. J. Xiao, Y. Xie, J. Liu, and M. Liu, "Deactivation of Nickel-Based Anodes in Solid Oxide Fuel Cells Operated on Carbon-Containing Fuels," *J. Power Sources*, **268** 508-16 (2014).
73. J.-H. Koh, Y.-S. Yoo, J.-W. Park, and H. C. Lim, "Carbon Deposition and Cell Performance of Ni-YSZ Anode Support SOFC with Methane Fuel," *Solid State Ionics*, **149** [3-4] 157-66 (2002).
74. M. K. Nikoo and N. A. S. Amin, "Thermodynamic Analysis of Carbon Dioxide Reforming of Methane in View of Solid Carbon Formation," *Fuel Process. Technol.*, **92** [3] 678-91 (2011).

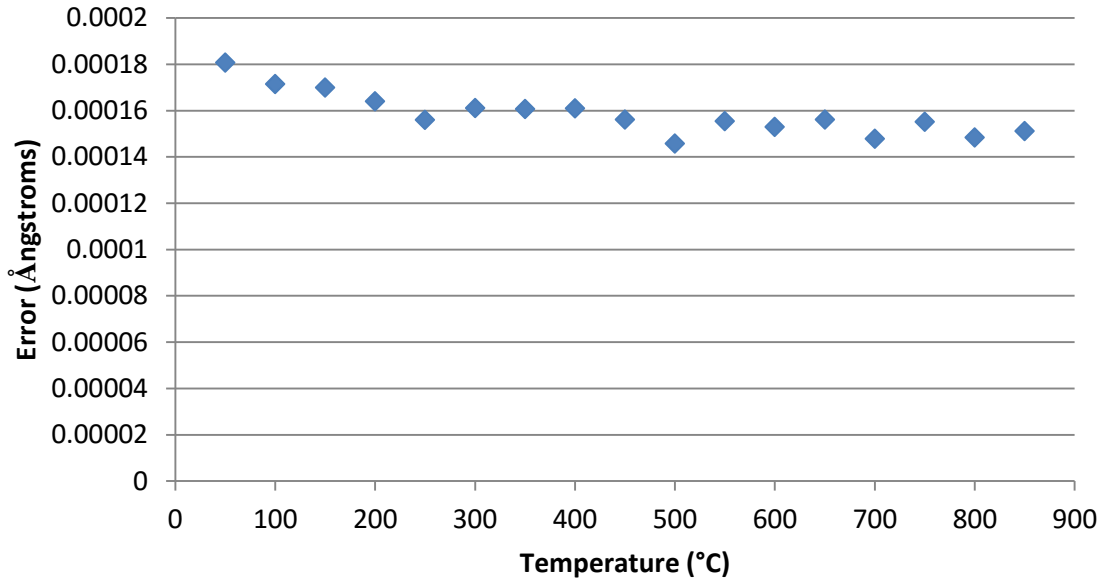
APPENDICIES

Appendix A. Ni_{0.375}Cu_{0.375}Mg_{0.25}Al₂O₄ XRD Pattern



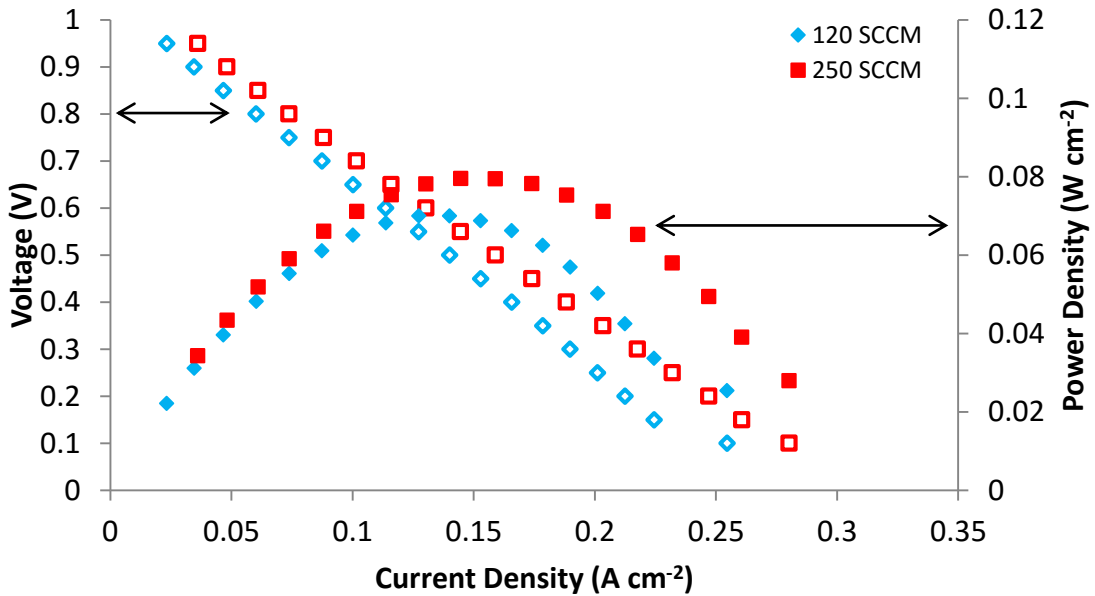
A-1. The XRD pattern for the synthesized $\text{Ni}_{0.375}\text{Cu}_{0.375}\text{Mg}_{0.25}\text{Al}_2\text{O}_4$ spinel.

Appendix B. Coefficient of Thermal Expansion

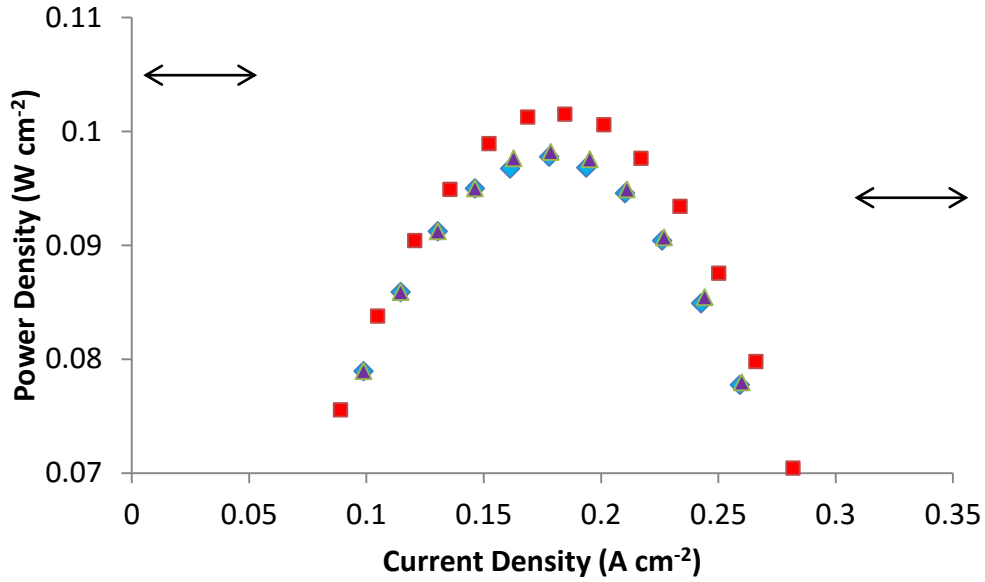


B-1. The calculated error, in Ångstroms, for each calculated a lattice parameter from Rietveld refinements.

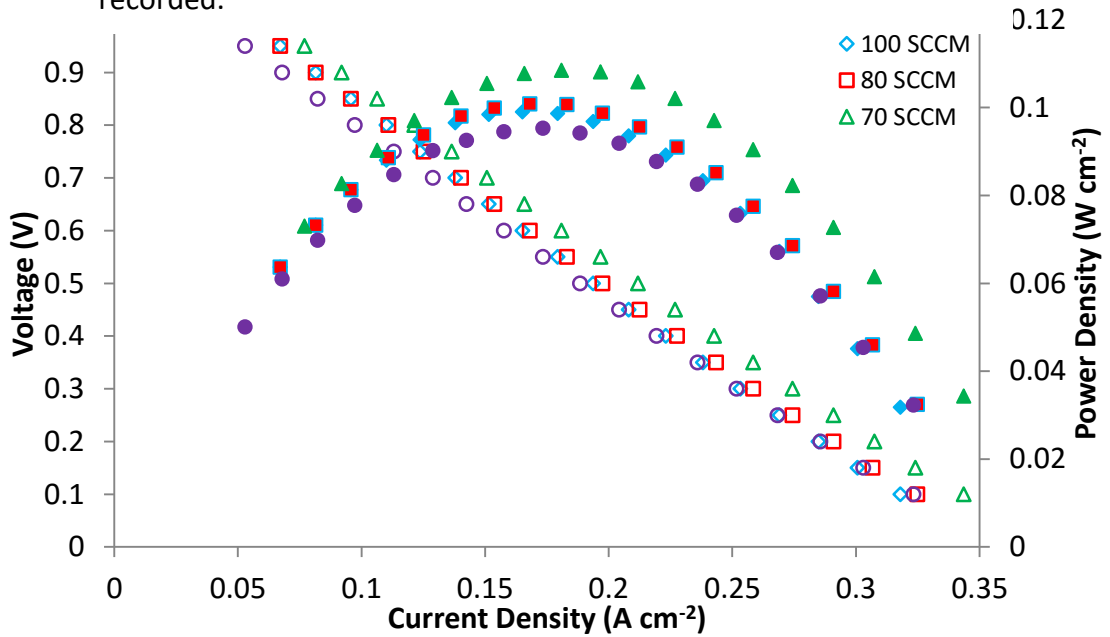
Appendix C. Electrochemical Performance Measurements



C-1. Gas flow rate effects for 4% H₂ fuel gas at 850°C.

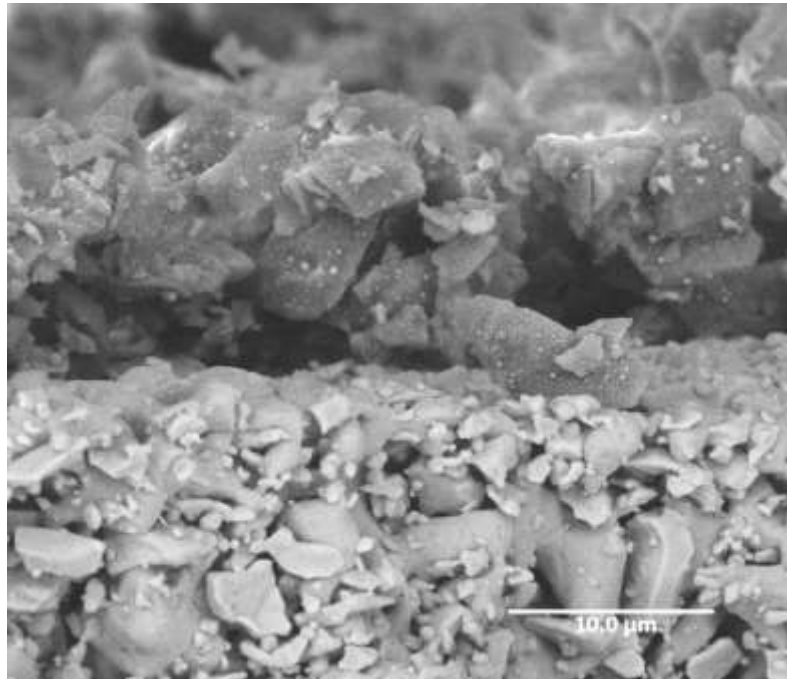


C-2. Current density vs power density plot for three consecutive measurements under 1 CH₄: 1 CO₂ fuel gas at 850°C. A 3.7 mW cm⁻² difference between the highest and lowest peak power density was recorded.

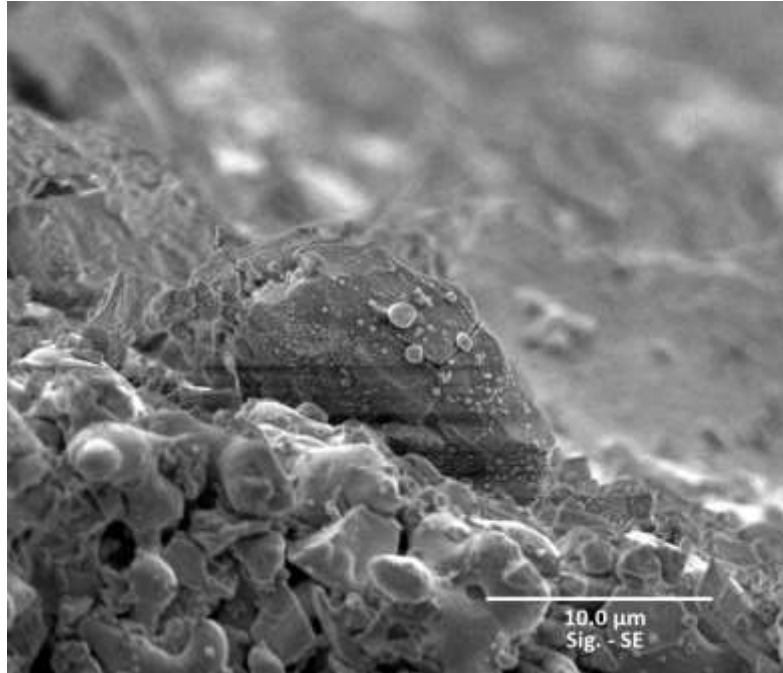


C-3. Fuel gas flow rate effects for 1 CH₄:1 CO₂ at 850°C.

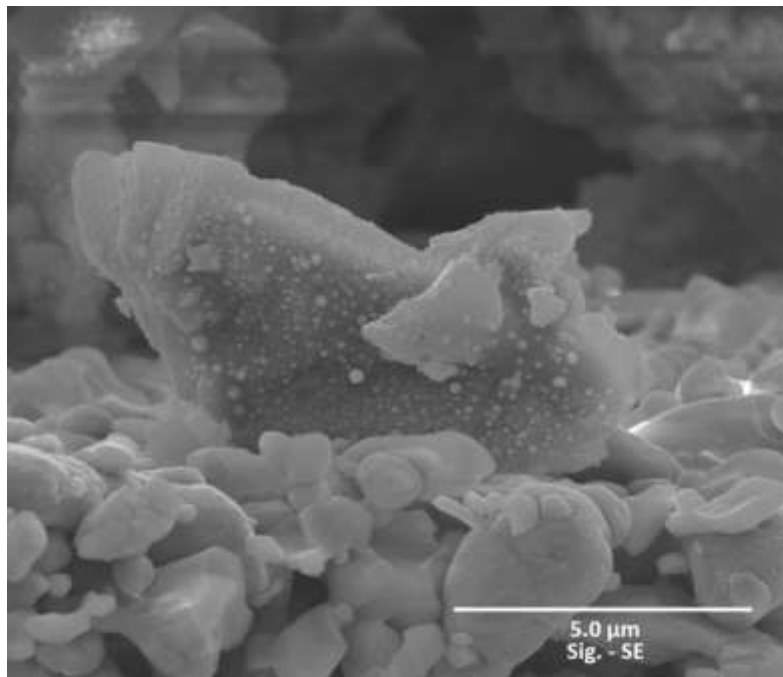
Appendix D. SEM Photomicrographs



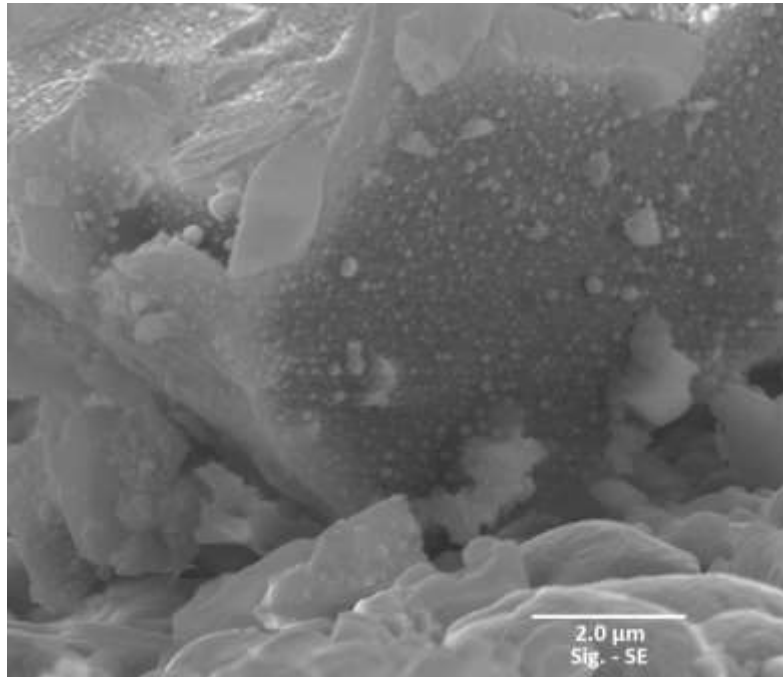
D-1. SEM image of 0.05g spinel addition sample post endurance testing. The spinel can be seen on top of the SOFC anode.



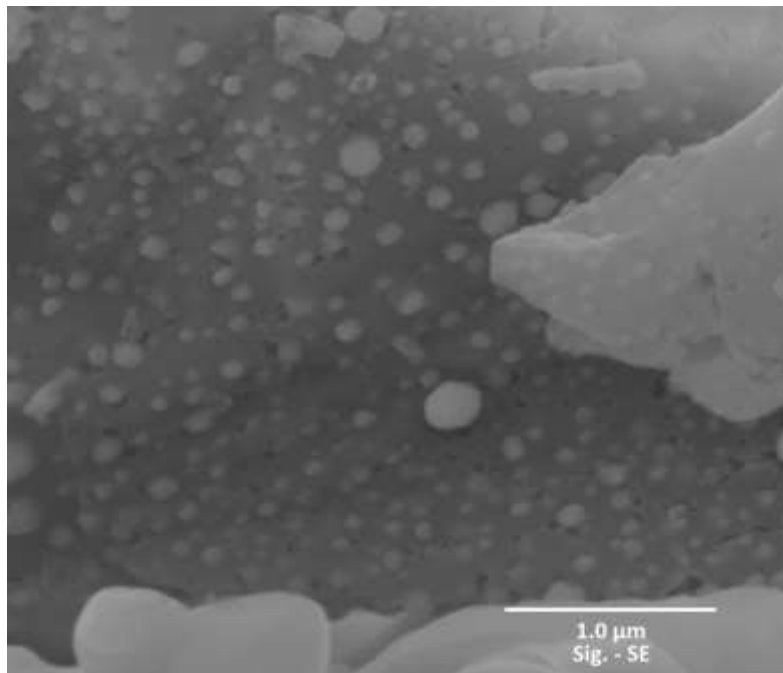
D-2. SEM image of 0.015 g of spinel addition sample post endurance testing. Nanoparticles can be seen on the spinel surface.



D-3. SEM image of 0.015g spinel addition sample. Ni-Cu alloy particles can be seen on the surface of the spinel particles.



D-4. SEM image of the interface between the spinel particles and the cermet anode.



D-5. SEM image of Ni-Cu nanoparticles reduced out of spinel. To alleviate the stress induced from the loss of Ni, pores and micro-cracks form on the spinel surface.

